FEDERAL UNIVERSITY OF SANTA CATARINA
TECHNOLOGY CENTER
AUTOMATION AND SYSTEMS DEPARTMENT
UNDERGRADUATE COURSE IN CONTROL AND AUTOMATION ENGINEERING

Luiz Fernando Martins Pastuch

Development of a Phenomenological Radar Model for Simulation of Advanced Driver Assistance Systems

Florianópolis
2020

Luiz Fernando Martins Pastuch

Development of a Phenomenological Radar Model for Simulation of Advanced Driver Assistance Systems

Final report of the subject DAS5511 (Course Final Project) as a Concluding Dissertation of the Undergraduate Course in Control and Automation Engineering at the Federal University of Santa Catarina in Florianópolis.
Advisor: Prof. Rodolfo César Costa Flesch, Dr.
Supervisor: Dirk Balzer, Dr. Eng.

Florianópolis
2020

NON DISCLOSURE AGREEMENT

This report contained confidential data from Opel Automobile GmbH. During a time period of 3 years, the publication or reproduction of the original work is not permitted. The original work may only be made available to the reviewers, the examination board and the people responsible for archiving at the university.

Thus, the presented report was prepared to contains only non-confidential data, to be available to the general public prior to the 3 year period, as required by the Federal University of Santa Catarina.

Rüsselsheim am Main, October 2020

ACKNOWLEDGEMENTS

First of all, I would like express my gratitude to Opel Automobile, for the great opportunity of internship in a worldwide company that was provided to me. The experience of working in the automotive industry was something I always craved for, and I will be forever grateful for that.

I would like to thank all the engineers at the Electric Power System & Controls Integration, and the Virtual Development & Test Automation departments, in special to my supervisors Dirk Balzer and Johannes Leuer, for their guidance, knowledge, and support throughout the entire development of this project.

I further extend my acknowledgment to Stefan Sinsel and all the engineers of the AXIOM team, for their welcoming into the team on the first part of my internship, and for their vast knowledge of model-based development, hardware communication, and real-time simulation, that proved essential during my time at the company.

My thanks to my university supervisor Prof. Rodolfo César Costa Flesch, for his support and his academic competence during this period.

Finally, my immense gratitude to my parents, Fernanda and Luciano, and to all my family and friends for their support during my time in Germany, making it all possible.

“The Universe
is simply a great machine
which never came into being
and never will end.”
(Tesla, 1937)

ABSTRACT

Testing of advanced driver assistance systems (ADAS) is highly demanding in time and equipment cost. As a solution, companies intend to migrate from prototype testing to simulation in virtual environments. The project described in this document is the development of a phenomenological radar model for simulation of ADAS, with the autonomous emergency braking (AEB) test protocol from European New Car Assessment Program (Euro NCAP) chosen as initial goal. To achieve a high level of realism in simulation, the model must be able to reproduce the expected system dynamics and phenomena related to non-idealities, such as noise, losses and faults. In addition, the radar target used for such tests must be properly characterized and modeled. The target, known as global vehicle target (GVT), was measured in field with proper radar equipment in an open area to investigate the variability and deterioration of its radar cross section (RCS). Gathered data led to the conclusion that the GVT displayed high RCS variability in a tolerable margin between different assemblies, but the impact on the RCS of repeated crashes on the target was inconclusive. Further, the functional phenomenological noisy (FPN) radar model is implemented in MATLAB/Simulink, supported by the integration with IPG CarMaker. The model uses a detection criteria based on the concept of signal-to-noise ratio (SNR) and its final output values are structured for integration with a bypass interface available in hardware-in-the-loop (HIL) platforms. As a result, the model displayed similar behavior to a different *off-the-shelf* phenomenological radar model during offline testing. In HIL simulations with an AEB controller, the resulting data pointed out slight differences in performance when using the FPN model and an ideal model, which can be considered as a first step towards a migration of only functional testing to performance testing via virtual simulation.

Keywords: Phenomenological. Radar. Modeling. Simulation. GVT. ADAS.

RESUMO

Testes de sistemas avançados de assistência ao motorista (ADAS, do inglês *advanced driver assistance systems*) são altamente exigentes em tempo e custo de equipamento. Como solução, montadoras buscam migrar de testes com protótipos para simulações em ambientes virtuais. O projeto descrito neste documento é o desenvolvimento de um modelo fenomenológico de radar para simulação de ADAS, com o protocolo de teste do sistema de frenagem automática de emergência (AEB, em inglês) do Programa Europeu de Avaliação de Novos Automóveis (Euro NCAP, em inglês) escolhido como meta inicial. Para se obter um alto nível de realismo em simulação, o modelo deve ser capaz de reproduzir dinâmicas esperadas do sistema e fenômenos relacionados à não-idealidades, como ruídos, atenuações e falhas. Além do mais, o alvo de radar usado em tais testes deve ser devidamente caracterizado e modelado. O alvo, conhecido como alvo veicular global (GVT, em inglês) foi medido em campo com equipamento de radar adequado em uma área aberta para investigar a variabilidade e deterioração de sua seção transversal de radar (RCS, em inglês). Os dados coletados levaram à conclusão de que o GVT exibiu alta variabilidade de RCS em uma margem tolerável entre diferentes montagens, mas o impacto no RCS de repetidas colisões no alvo foi inconclusivo. Mais além, o modelo funcional-fenomenológico-ruidoso (FPN, em inglês) de radar é implementado em MATLAB/Simulink e amparado por uma integração com IPG CarMaker. O modelo usa um critério de detecção baseado no conceito de relação sinal-ruído (SNR, em inglês) e seus sinais de saída são estruturados para uma integração com uma interface de *bypass* disponível em plataformas de *hardware-in-the-loop* (HIL). Como resultado, o modelo demonstrou comportamento similar à outro modelo fenomenológico comercial de radar durante testes isolados. Em simulações HIL como um controlador de AEB, os dados resultantes apontaram pequenas diferenças no desempenho ao usar o modelo FPN e um modelo ideal, o que pode ser considerado como um primeiro passo para a migração de apenas testes funcionais para testes de desempenho por meio de simulação virtual.

Palavras-chave: Fenomenológico. Radar. Modelagem. Simulação. GVT. ADAS.

LIST OF FIGURES

LIST OF TABLES

LIST OF ABBREVIATIONS AND ACRONYMS

3-D	three-dimensional
ACC	adaptive cruise control
ADAS	advanced driver assistance systems
AEB	autonomous emergency braking
CCRm	car-to-car rear moving
CCRs	car-to-car rear stationary
CM	CarMaker
CSV	comma-separated values
EBT	Euro NCAP bicyclist and bike target
ECU	electronic control unit
EPT	Euro NCAP pedestrian target
ESC	electronic stability control
Euro NCAP	European New Car Assessment Programme
FA	fixed-angle
FPN	functional phenomenological noisy
FR	fixed-range
GVT	global vehicle target
HiFi	high fidelity
HIL	hardware-in-the-loop
LCV	light commercial vehicle
MIL	model-in-the-loop
PDF	probability-density function
RCS	radar cross section
SNR	signal-to-noise ratio
TTC	time to collision
VRU	vulnerable road user
VUT	vehicle under test
XCP	universal measurement and calibration protocol

CONTENTS

1 INTRODUCTION

This work describes the development of a phenomenological radar model in a virtual environment as part of a project developed in the Electric Power System & Controls Integration department of Opel Automobile GbmH for simulation of autonomous emergency braking (AEB) assessment tests. Furthermore, the work describes the investigation of radar characteristics of a global vehicle target (GVT), also part of the assessment tests.

1.1 THE COMPANY

Opel Automobile GmbH is a German automobile manufacturer based in Rüsselsheim am Main, Hesse. The company traces its roots to a sewing machine manufacturer founded by Adam Opel in 1862, and produced its first automobile in 1899, designed by Adam's widow Sophie Marie Opel and her sons.

The company has ten factories and four development sites in six European countries, selling around one million vehicles yearly. It has 37,000 employees in total, and around 6,250 are responsible for the engineering and design of Groupe PSA vehicles at the International Technical Development Center and European Design Center, also based in Rüsselsheim.

Figure 1 – Opel logotype.

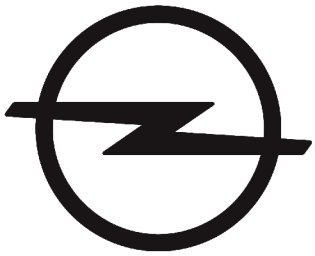

Source – Opel Pressroom (2017).

Opel's slogan "*Die Zukunft gehört allen*" (The future is everyone's, in English) reflects its philosophy that technology and innovation have the power to change lives and why it should be available for the maximum possible number of people. This purpose is deeply rooted in the brand DNA.

Opel remained part of the General Motors Company for 88 years, from 1929 until 2017, when it was sold for the Groupe PSA for US$2.2 billion. Shortly after the acquisition, Michael Lohscheller (CEO of Opel) presented PACE!, the Opel-Vauxhall strategic plan to restore financial fundamentals and enhance sustainable competitiveness and growth for the brand.

In short, the PACE! plan focused on improving efficiency towards benchmark levels for manufacturing and logistics costs, enlarging Opel's light commercial vehicle (LCV) business, and Electrification and CO_2 leadership, with the target of all passenger car lines to be electrified by 2024.

As stated in the 2019 Financial Report of Groupe PSA [1], Opel achieved a record 1.1 billion Euros of adjusted operating income and 6.5% adjusted operating margin in that year, a goal set only for 2026. PACE! is working, and that is more important than ever, given the stormy situation the automotive industry is experiencing worldwide, due to stricter pollution laws, saturated markets, and new urban mobility solutions.

1.2 MOTIVATION AND JUSTIFICATION

Advanced driver assistance systems (ADAS) are electronic systems designed to support the driving task, ranging from simple information presentation and warning sounds up to taking over the driver's tasks in a critical situation. In [2], ADAS are defined as vehicle-based intelligent safety systems which could improve road safety in terms of crash avoidance, crash severity mitigation and protection and post-crash phases.

The system covered in this project — Autonomous Emergency Braking (AEB) — assists by preventing traffic accidents or reducing the severity of impact, if deemed as eminent. Such system collects and analyses surrounding environment information to detect approaching vehicles or other road objects using sensors such as radar, camera and lidar, and acts by applying braking when necessary. A study developed with data from six countries concluded that vehicles equipped with AEB systems were effective in preventing 38% of front to rear collisions [3].

Nowadays, a wide variety of ADAS technologies are in use, some of which are increasingly fitted to vehicles as standard equipment. Research on brake assistance, electronic stability control (ESC) and adaptive cruise control (ACC) also indicates that these measures offer significant safety potential [4], [5].

The increase in adoption of ADAS by the automotive industry raised the necessity of assessment and homologation of these technologies. As stated in [6], if testing and assessment methods cannot keep pace with this functional growth, they will become the bottleneck of the introduction of ADAS to the market.

Initiatives such as the European New Car Assessment Programme (Euro NCAP) responded with development of new rating systems, test procedures and standards for evaluation [7]. In 2009, Euro NCAP adopted a single overall safety rating with a maximum of five stars for each vehicle, which is a result of the combined assessment results of four areas: Adult Occupant Protection, Child Occupant Protection, vulnerable road user (VRU) Protection, and Safety Assist (driver-assistance and crash-avoidance technologies).

Euro NCAP tests protocols are not only an end-result evaluation procedure but have also been used by the automotive industry as means of directly improving safety by taking part in the vehicle and ADAS development process. For AEB systems, there are two protocols: AEB Car-to-Car systems [8], concerning the test procedures with another vehicle and part of the Safety Assist assessment, and AEB VRU Systems [9], concerning the test procedures with pedestrians and bicyclists, part of the VRU Protection assessment.

In addition, the surrogate targets for pedestrians, bicyclists, and vehicles to be used for assessment are also specified in [10], [11], and [12], respectively. The Euro NCAP pedestrian target (EPT), Euro NCAP bicyclist and bike target (EBT), and global vehicle target (GVT) are designed to replicate the visual, radar and lidar attributes expected from each kind, while minimizing potential damage and risk to the vehicle under test (VUT) and its occupants.

Both AEB test protocols are currently part of the development process at Opel. Yet, such tests are highly demanding in terms of staff, equipment cost, and dedicated time to plan and execute, given that each protocol requires several different ways of approach between VUT and target — varying relative speed, lateral overlap, and target maneuver — and measuring equipment, test track, and weather must fit specific conditions and requirements.

There is great interest to obtain a simulation of Euro NCAP AEB tests in order to reduce costs, time and environment variability in early development phases for functional testing. Furthermore, the goal is to provide a good base for an increase of performance evaluation of software and hardware prototypes via simulation, if models with a high fidelity level are used in the application.

The AEB Car-to-car protocol was chosen as an initial target, as it is relatively simpler to reproduce in a virtual environment than the AEB VRU protocol. The latter requires set-ups with two distinct targets (EPT and EBT) in several different scenarios, some with additional vehicles to create blind-spot situations, while the car-to-car protocol has only one target (the GVT) and all tests are performed in a clean scenario with no additional vehicles. Thus, it is a good starting point for the project, to later enhance with the addition of the VRU protocol.

In order to achieve a high level of fidelity or resemblance to reality in simulation, models to be used must be able to reproduce expected system dynamics while encompassing phenomena related to non-idealities, such as noise, losses and faults. Therefore, key components of the assessment test — chassis, brake & hydraulics, tires, CAN network, radar, camera, and GVT — are tackled by a team of specialists in the respective areas during the model development process.

1.3 OBJECTIVES

The main objective of this work is to obtain a functional phenomenological noisy (FPN) radar model. Such model must acquire environment information and consider object specific characteristics to infer if it is detected or not. Additionally, an FPN must be extendable, to allow new effects seen on proving grounds to be added without much integration effort.

Another objective is to characterize the global vehicle target (GVT) in the simulation environment, regarding its radar attributes. For that purpose, a specific goal is to measure such attributes in field and to observe and investigate changes due to intensive use (referred to in this document as “aging”).

1.4 DOCUMENT STRUCTURE

This monograph is organized as follows:

- **Chapter 2** presents the required technical concepts to better comprehend the covered topics;
- **Chapter 3** provides a review of the available literature of the approached topics and describes the intended goals of the investigation of the GVT and the development of the FPN model, with desired structure and effects.
- **Chapter 4** describes the work performed to obtain and analyze measurement data and concludes over the characteristics of the GVT;
- **Chapter 5** describes the modeling process of the FPN model in the virtual environment.
- **Chapter 6** displays and analyses the obtained simulations results, in a comparison with other radar models and in a hardware-in-the-loop (HIL) application.
- **Chapter 7** presents the concluding remarks and future perspectives.

2 RADAR FUNDAMENTALS

This chapter covers the necessary topics for a better understanding of the subsequent chapters. It provides an introduction to radar systems, regarding working principles and theoretical equations, to clarify key topics for the comprehension of this work.

2.1 RADAR SYSTEMS

Radar — formerly an acronym for *Radio Detection And Ranging* — is a detection and tracking system based on the reflection of electromagnetic waves on another object. Radar systems are used to detect ships, aircraft, weather formations and terrain, and in recent years, also started to play a role in the detection of road objects and vehicles in ADAS.

Figure 2 – Basic working principle of radar.

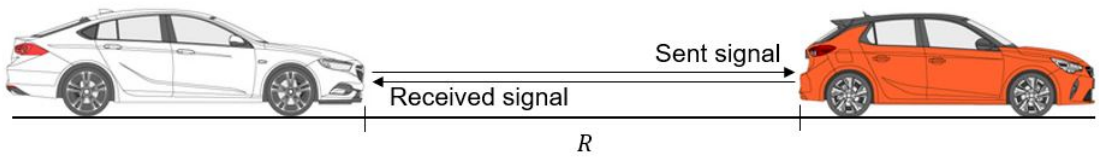

Source – Personal Archive (2020).

One of the main function of radar in ADAS is to obtain the distance or range R to the target, visible in Figure 2. Yet, the technique used to obtain it is different for each type of radar. On *Pulse-Doppler* radars, it is done by measuring the time difference Δt between the moment a signal is transmitted and the moment an echo signal is received. With that, the range can be calculated based on the time difference and the speed of propagation c of the electromagnetic wave using the equation

$$R = c\frac{\Delta t}{2} \, . \tag{1}$$

On the other hand, *frequency-modulated continuous wave (FM-CW)* radars operate by transmitting and receiving at the same time. A systematic variation of transmitted frequency places a unique time stamp on the transmitted wave at every instant and, by measuring the frequency of the received signal, the range R is given by

$$R = c\frac{T}{2}\frac{\Delta f}{f_2 - f_1} \, , \tag{2}$$

where Δf is the difference between the transmitted and received signals, f_2 is the maximum transmitted frequency, f_1 is the minimum transmitted frequency, and T is the period between f_1 and f_2.

In addition to range, additional information of the target can be obtained by observing a series of amplitude and phase measurements as a function of time, frequency, and position [13]. The measurements of angular direction, range, and Doppler velocity may be derived from the variation of phase ϕ with time t, frequency f, and position x. Further, measurements of target shape, size, and rotation may be derived from the variation of the amplitude A, although these are rarely used in radar applications. In summary:

- $\left(\frac{\partial \phi}{\partial x}\right)_{t,f} \rightarrow$ angle
- $\left(\frac{\partial \phi}{\partial t}\right)_{x,f} \rightarrow$ relative velocity
- $\left(\frac{\partial \phi}{\partial f}\right)_{t,x} \rightarrow$ range
- $\left(\frac{\partial A}{\partial x}\right)_{t,f} \rightarrow$ shape
- $\left(\frac{\partial A}{\partial t}\right)_{x,f} \rightarrow$ rotation
- $\left(\frac{\partial A}{\partial f}\right)_{t,x} \rightarrow$ size

The following subsections present the theory to obtain the radar equation and to define the concepts of radar cross section, antenna gain and signal-to-noise ratio, a central part of the work presented in the next chapters.

2.1.1 The Radar Equation

When using an omnidirectional antenna, which radiates uniformly in all directions, the power density at a distance R from the radar is equal to the transmitter power P_t divided by the surface area $4\pi R^2$ (considering isotropic or spherical radiation), or

$$P_{oa} = \frac{P_t}{4\pi R^2} \ , \tag{3}$$

where P_{oa} is the power density from an omnidirectional antenna. Yet, radars usually employ directive antennas to channel most of the radiated power P_t into some particular direction. The transmission gain G_t of an antenna is a measure of the increased power radiated in the direction of the target as compared with the power that would have been radiated from an isotropic antenna [13]. The power density P_{da} from a directive antenna with a transmitting gain G_t is

$$P_{da} = \frac{P_t G_t}{4\pi R^2} \ . \tag{4}$$

The target, on the other hand, intercepts only a portion of the radiated power and

re-radiates it in the direction of the radar as

$$P_{re} = \frac{P_t G_t \sigma}{4\pi R^2} \ . \tag{5}$$

where P_{re} is the power re-radiated in the target direction [13].

In Equation (5), the Greek letter σ represents the radar cross section (RCS) of the target. The RCS is a characteristic of the target and is a measure of its size as seen by the radar. The power density in the echo signal P_{es} at the radar receiving antenna is then

$$P_{es} = \frac{P_t G_t \sigma}{(4\pi R^2)^2} \ . \tag{6}$$

The radar antenna then captures a portion of the echo power. If the effective capture area of the receiving antenna is A_r, the echo power P_r received at the radar is

$$P_r = \frac{P_t G_t A_r \sigma}{(4\pi R^2)^2} \ , \tag{7}$$

considered to be the fundamental form of the radar equation [13]. Furthermore, antenna theory provides the relationship between the antenna gain and its effective area as

$$G_t = \frac{4\pi A_t}{\lambda^2} \quad \text{and} \quad G_r = \frac{4\pi A_r}{\lambda^2} \ , \tag{8}$$

where the subscripts r and t refer to the receiving and transmitting antennas, respectively. If a single antenna is used for both transmission and reception (as is usually the case), the reciprocity theorem states that $G_t = G_r = G$ and $A_t = A_r = A$. Using these relationships, Equation (7) becomes

$$P_r = \frac{P_t G^2 \lambda^2 \sigma}{(4\pi)^3 R^4} \ . \tag{9}$$

It is important to state that Equation (9) is not capable to describe radar performance in practical radars with absolute precision. Because of the implicit nature of relationships between the parameters that appear in the radar equation, one must be careful about making generalizations concerning radar performance on the basis of these equations alone. However, it may provide a good basis for a simplified mathematical modeling of radar systems.

2.1.2 Radar Cross Section

The radar cross section (RCS) of a target, often represented by σ, is the area that, when intercepting an amount of power, reflects a portion of the received power and produces an echo at the radar equal to that from the target [13]. In other terms,

$$\sigma = 4\pi \lim_{R\to\infty} R^2 \left|\frac{E_r}{E_i}\right|^2 , \tag{10}$$

where R is the distance between radar and target, E_r is the reflected field strength and E_i is the incident field strength. For most radar targets, the RCS does not have a simple relationship to the physical area, except that the larger the target size, the larger σ is likely to be.

A portion of the incident energy received by a target is absorbed as heat, while the remainder is scattered in many different directions, depending on its shape and orientation in relation to the source of the electromagnetic wave. The portion of the re-radiated energy scattered or reflected is of chief interest in radar.

Usually, the RCS is based on an area of 1 m^2 and is stated in dB as

$$\sigma / \mathrm{dBm}^2 = 10 \log_{10}\left(\frac{\sigma}{1\ \mathrm{m}^2}\right) . \tag{11}$$

In other words, the RCS (or σ) of a target is the effective area A_{eff} of metal sphere (where $A_{eff} = \pi r^2$) which would return the same amount of power to the radar as the actual target [14].

2.1.2.1 RCS of Simple Objects

In theory, the scattered field, and hence the radar cross section, can be determined by solving Maxwell's equations with the proper boundary conditions applied [13]. Unfortunately, the determination of the RCS with Maxwell's equations can be accomplished only for simple shapes, and solutions valid over a large range of frequencies are not easy to obtain.

2.1.2.1.1 Sphere

The sphere is the simplest available scattering body, given that it offers the same view from all approaching directions, the scattering is independent on the target orientation (or aspect angle). The RCS of a sphere, when its radius r is much bigger than the wavelength ($r >> \lambda$), is simply given by

$$\sigma = \pi r^2 . \tag{12}$$

2.1.2.1.2 Trihedral Angle Reflector

Trihedral angle reflectors, shown in Figure 3, are objects able to generate relatively strong echoes despite having a small reflective area. They consist of three electrically conductive surfaces, mounted with a 90° angle between then, which makes every wave reflected by the surface to be in parallel with the incident wave.

Figure 3 – Trihedral angle reflector.

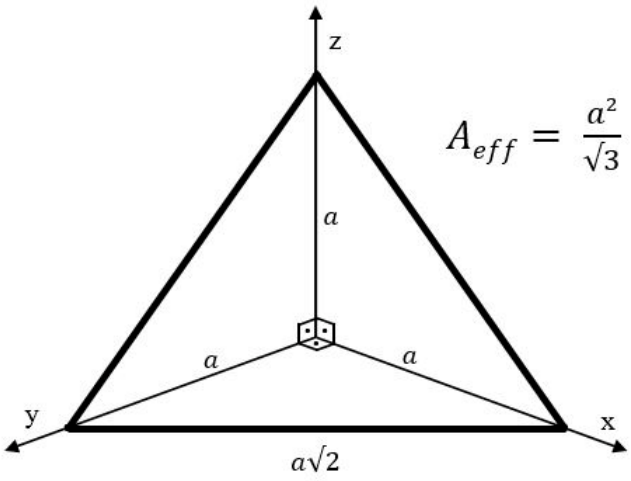

Source – Personal Archive (2020).

A trihedral with three triangular reflective surfaces — when facing the radar directly — has an RCS given by

$$\sigma = \frac{4\pi a^4}{3\lambda^2} \ . \tag{13}$$

To illustrate the effect of such reflectors on radar, a trihedral with a = 0.1 m has an effective area A_{eff} of only 0.0057 m^2. Yet, considering a radar operating in a frequency of 77 GHz (λ = 3.89 mm), the object has a RCS of 27.59 m^2, or 14.4 dBm^2, a usual value for a passenger vehicle.

2.1.2.2 RCS of Complex Objects

Vehicles, airplanes and ships are considered complex objects for radar systems. These objects have several scattering centers that make up to a very irregular RCS pattern. To calculate a theoretical RCS is very difficult and requires a considerable effort. Therefore, other ways such as original measurement, model measurement, simplification or concentration on area of interest for calculation are normally chosen as a solution [13].

As an example, Figure 4 shows a radar back-scattering diagram (or simply *RCS map*) of a standard passenger vehicle. Such diagrams are a display of the RCS magnitude vs. Aspect Angle. For the diagram in question, the vehicle was measured at a 30 m distance with a radar operating at 77 GHz. The front-side of the car is considered to be an aspect angle of 0°.

Figure 4 – RCS map of a passenger vehicle.

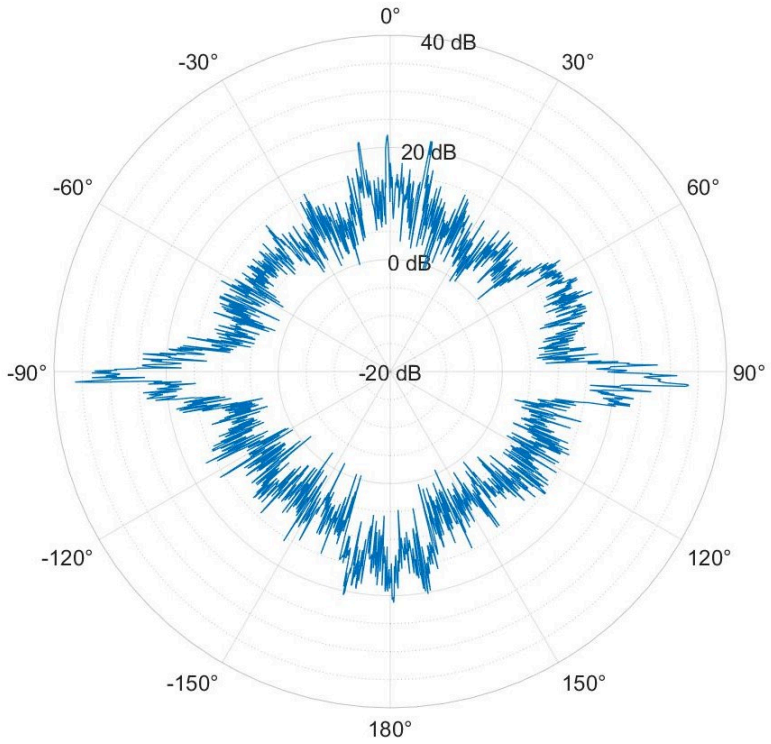

Source – Personal Archive (2020).

The large fluctuations in the RCS values shown are mainly due to the different shapes and angles that make up the vehicle body. At certain aspect angles, the vehicle surface is orthogonal to the incident wave, while at others the orientation and shape is such that scatters the waves to several different directions. This led to peaks of around 35 dBm^2 at $\pm 90°$ (side parts of the vehicle) while having valleys near 0 dBm^2 at $\pm 30°$ (front corners of the vehicle, with a more rounded shape).

2.1.3 Antenna Parameters

Almost all radars use directive antennas for transmission and reception. This kind of antenna channels the radiated energy into a beam to enhance the energy concentrated in the direction of the target on transmission. The antenna gain G is a

measure of the power radiated in a particular direction by a directive antenna to the power which would have been radiated in the same direction by an omnidirectional antenna with 100% efficiency [13]. In other words, the gain of an antenna is

$$G(\varphi, \theta) = 4\pi \frac{P_{ra}(\varphi, \theta)}{P_a} \ . \tag{14}$$

where $P_{ra}(\varphi, \theta)$ is the power radiated per unit solid angle in azimuth φ and elevation θ, and P_a is the power delivered to the antenna.

The antenna gain is a function of direction. Based on the principle of the conservation of energy, if it is greater than unity in some directions, it must be less than unity in other directions. Figure 5 shows the diagram for a generic antenna on a horizontal section with elevation $\theta = 0°$, or $G(\varphi, 0°)$.

Figure 5 – Gain diagram of a generic antenna.

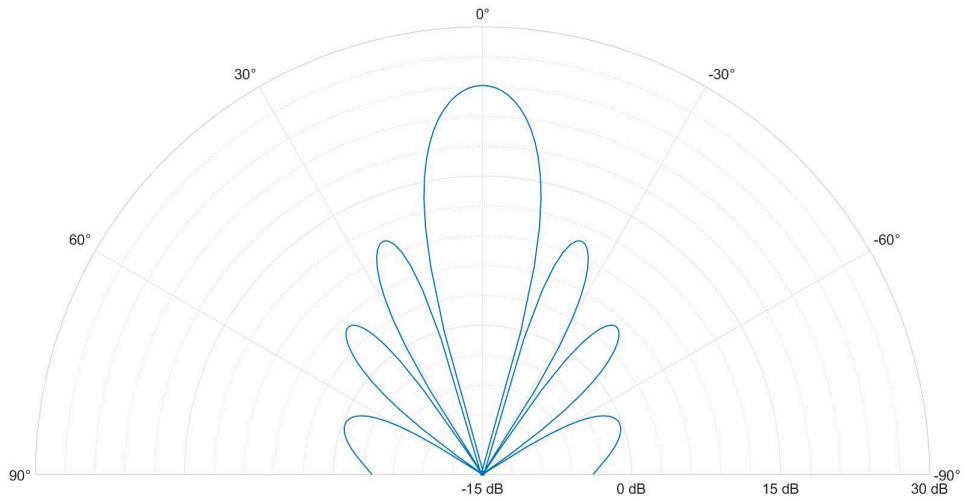

Source – Personal Archive (2020).

As previously mentioned in Subsection 2.1.1, one of the principles of antenna theory is *reciprocity*, which states that the properties of an antenna are the same regardless whether it is used for transmission or reception. Therefore, the gain of a transmitting antenna is the same as the one observed when the antenna is used for receiving.

2.1.4 Detection Threshold and Signal-to-Noise Ratio

The ability of a radar receiver to detect a weak echo signal is directly related to the noise amid the echo. The weakest signal the receiver can detect is called the minimum detectable signal. Its specification is sometimes difficult, given the statistical

nature of noise, thus making the criteria to decide if a target is or is not present not too well defined [13].

Detection is based on establishing a threshold level for the receiver. If the output exceeds the threshold, a target is assumed to be present. If the minimum detectable signal (or threshold level) is set sufficiently high, the receiver output would not exceed the threshold if noise alone is present, but would exceed it in case of a strong signal. However, if the signal is small, it would be much more difficult to recognize its presence. In summary, the threshold level must be low if weak signals are to be detected, but it cannot be so low that noise peaks cross the threshold and give a false indication of the presence of targets.

By nature, noise is a random phenomenon. Predictions concerning the average performance of chance events are possible by observation and analysis of occurrences, but one cannot predict exactly what will occur for any particular event. Yet, such phenomena of a random nature can be described with the assistance of probability theory, and one of its most useful concepts needed to analyze the detection of signals in noise is the probability-density function (PDF) [13].

A PDF is a function whose value at any given sample, in the set of possible values taken by the random variable, provides the likelihood that the value of the random variable would equal the sample.

The probability-density function $p\{x)$ is defined as

$$p(x) = \lim_{\substack{\Delta x \to 0 \\ N \to \infty}} \frac{N_x/\Delta x}{N} \ , \tag{15}$$

where N_x is the number of values in range Δx at x, and N is the total number of values. The probability P that the value of x is in the finite range from x_1 to x_2 is found by the integration of $p(x)$ over the interval, or

$$P(x) = \int_{x_1}^{x_2} p(x)dx \ . \tag{16}$$

The Gaussian probability density function, also known as normal PDF, is one of the most important in noise theory, since many sources of noise, such as thermal noise or shot noise, may be represented by Gaussian statistics. This PDF has a bell-shaped appearance (shown in Figure 6) and is defined by

$$p(x) = \frac{1}{\sqrt{2\pi\sigma^2}} \exp\left(\frac{-(x-x_0)^2}{2\sigma^2}\right) \ , \tag{17}$$

where *exp*() is the exponential function, σ is the standard deviation, and x_0 is the mean value of the samples.

The *central limit theorem* states that the PDF of the sum of a large number of independently distributed quantities, such as signal noise, approaches the Gaussian PDF no matter what the individual distributions may be, provided that the contribution of any one quantity is not comparable with the resultant of all others [13].

Figure 6 – Gaussian probability-density function.

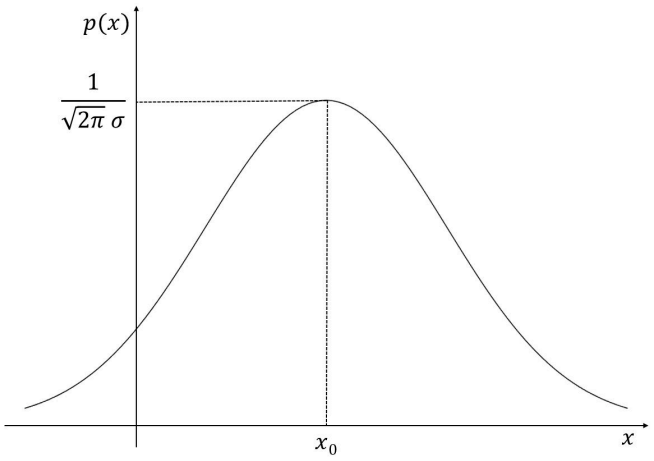

Source – Personal Archive (2020).

Another property of the Gaussian distribution is that no matter how large a value x may be, there is always a probability of finding a greater value. So, if the noise at the input of the threshold detector is truly Gaussian, then no matter how high the threshold is set, there is also a chance that it would be exceeded by noise and appear as a false alarm. Yet, the probability diminishes rapidly with increasing x, and the probability of obtaining an exceedingly high value of x is negligible and may be considered as *almost* impossible.

For the detection of radar targets, a compromise between a probability of false alarm P_{fa} (or "false alarm rate") and the probability of detection P_d is needed. The optimal threshold must be determined upon the respective application. A high threshold value leads to a small probability of false alarm, however, at the same time leads to a reduced probability of detection.

One may apply probability theory to obtain the signal-to-noise ratio (SNR) necessary to achieve a specified probability of detection without exceeding a specified probability of false alarm. The SNR is simply defined as the received signal power S divided by the noise power N, or

$$\text{SNR} = \frac{S}{N} \,. \tag{18}$$

Indirectly, it implies that given a certain noise level, *a minimum signal-to-noise ratio*

(SNR_{min}) may be chosen, thus setting a detection threshold, to achieve a balance between the probability of false alarm and the probability of detection.

Figure 7 – Probability of detection as a function of SNR and probability of false alarm.

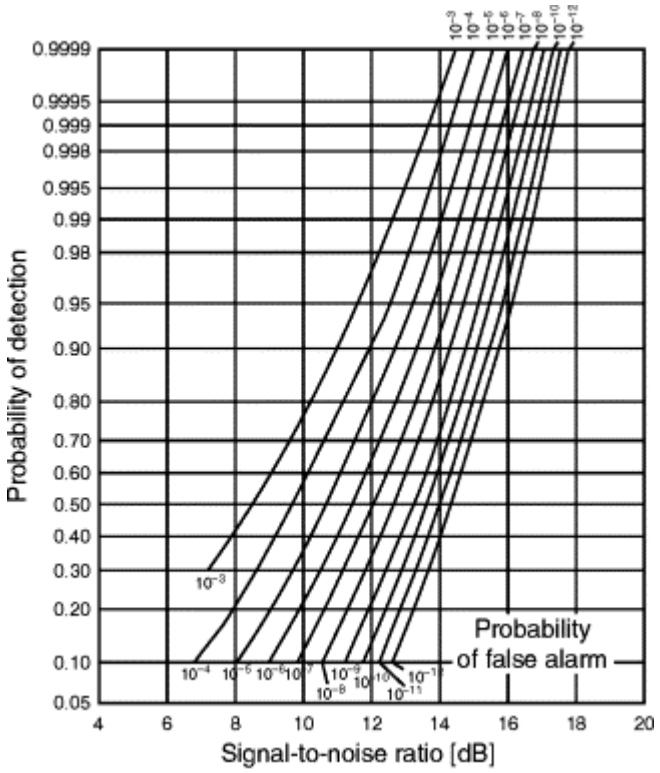

Source – The Electrical Engineering Handbook [15] (2005).

A diagram such as the one displayed in Figure 7 helps the radar engineer to reach the desired compromise for the detection threshold to be set. It shows the probability of detection P_d for a sine wave in noise as a function of the SNR and probability of false alarm P_{fa}. At first, it might seem that the SNR required for detection is higher than what we would guess by intuition, even for a P_d = 0.5. One might say that as long as the signal is greater than noise, detection should be accomplished. But when the probability of false alarm is taken into account, such statement may not be correct.

2.2 FINAL COMMENTS

The topics covered in this Chapter proved to be essential for the comprehension of radar systems and throughout the entire development of this work. Key concepts such as radar cross section, antenna characteristics, probability-density functions, and signal-to-noise ratio were then applied in the modeling process of the radar model. The next Chapter introduces the challenges regarding ADAS simulation, focusing on radar systems.

3 PROBLEM DESCRIPTION

In this section the problem is described and solutions are discussed. Section 3.1 illustrates the general problematic of ADAS simulation, with Subsections 3.1.1 and 3.1.2 addressing specific issues regarding radar systems and the GVT, respectively. Next, the solution for each problem is presented and the intended goals are set in Section 3.2, with an investigation of the GVT characteristics proposed in Subsection 3.2.1 and the definition of the phenomenological radar model made in Subsection 3.2.2.

3.1 SIMULATION OF ADVANCED DRIVER ASSISTANCE SYSTEMS

Over the past years, there has been a noticeable increase in the presence of advanced driver assistance systems (ADAS) in passenger vehicles and are said to be one of fastest growing areas in the automotive industry [16]. Currently, ADAS is finding its way from high-end luxury vehicles into more popular cars, not only leading to a bigger fleet equipped with this technology but also increasing spending, as shown in Figure 8, and expanding the variety of functions being introduced to the market every year.

Figure 8 – Manufacturer's spending on ADAS.

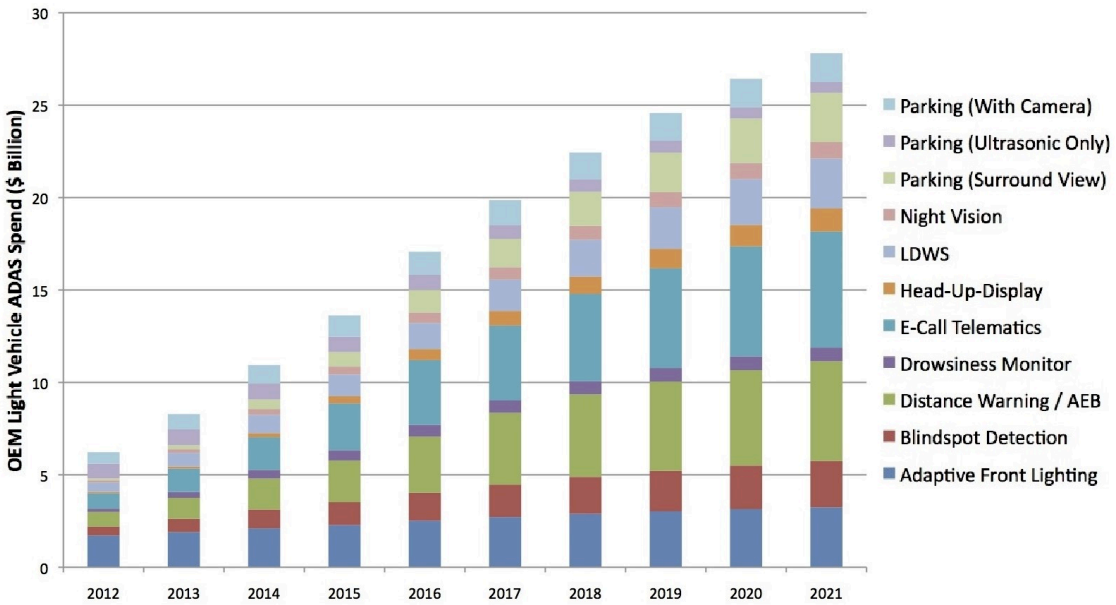

Source – Strategy Analytics / Edge AI + Vision Alliance [16] (2015).

The rapid growth of demand for the development of ADAS forced manufacturers to seek alternatives for testing and validation of new features and components. These systems have an immense workspace and have to be tested in a variety of complex traffic scenarios. Such versatility makes testing in real world scenarios hard,

if not impossible, given the difficulty to create different object interactions and weather conditions in a reproducible manner [17].

System engineers have resorted to simulation in an attempt to coupe with shorter deployment schedules and to achieve a more efficient and cost-effective development model. As discussed in [18], simulations can be used at different integration levels during the whole development process and facilitates repeatable test runs and traceable evaluation.

At Opel, simulations are widely used for functional validation in early integration phases, not only in ADAS development, but in several other applications of embedded systems. However, ADAS raised the need for the introduction of simulation in stages of performance testing.

As previously mentioned in Section 1.2, the work presented in this report is part of a project for simulation of Euro NCAP AEB assessment tests, which could be seen as a preliminary step for a steady increase of performance evaluation and validation via virtual testing in the development process.

One of the challenges for the simulation of ADAS is that it requires the coupling of accurate models from different domains. As for AEB, vehicle dynamics, including chassis, brakes and tire models, need to be coupled with environment perception sensor models, in this case, camera and radar. The latter is the main focus of this work, and it presents particular challenges in its modeling, as discussed in Section 3.1.1.

3.1.1 Radar Modeling

For the purpose of having meaningful results in simulation of ADAS, perception sensor models, such as radar, must achieve a sufficient level of realism. These models play a central role, as an interface between the vehicle under test (VUT) and the simulation environment.

However, there are no standard degree of fidelity or common interfaces for radar models, as they and are normally tailored to fit specific applications in model-in-the-loop (MIL) or HIL simulations, as pointed out by [19]. Often, radar models are tightly linked to their simulation environment, that not only limits the output accuracy of the model, but also hinders model interchangeability.

In reality, radar models display several effects and non-idealities, such as multi-path propagation, signal attenuation, occlusion, and measurement noise. The accuracy of how these effects are encompassed in the model has a direct influence in parametrization complexity and computational cost [20]. This trade-off results in several different modeling approaches, in an attempt to balance realistic representation and model complexity.

Figure 9 illustrates the different modeling approaches. The first approach is refereed as ground-truth model. These models have low realism and complexity and

are often employed in functional testing. They gather exact information directly from the simulation environment and output it as an object list, with no detection fault or measurement errors. Although ground-truth models lack the effects and characteristics of the real sensor, they are easy to parametrize and have little effect in computational speed [19].

Figure 9 – Compromise of complexity and realism in different approaches.

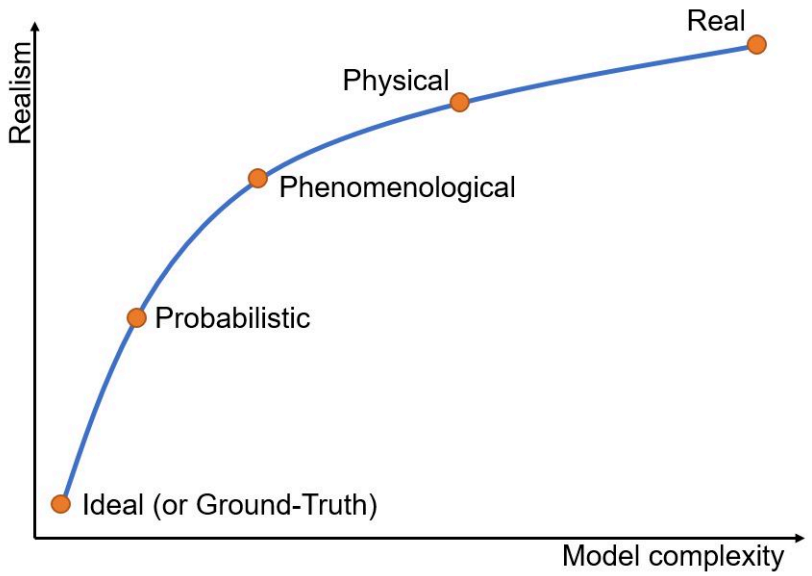

Source – dSPACE Magazine (2019).

Probabilistic or data-driven models may be seen as black-boxes, that seek to approximate the model outputs with real radar measurements by using data correlation and probability theory to create a state-space model. In a broad sense, for each simulated situation, similar recorded situations are identified. The simulated measurement should then be close to the recorded measurements in the identified situations. The models presented in [21], [22] displayed good results, however, data-driven models require a huge amount of representative recorded data to be trained to encompass non-idealities and are difficult to scale, as they need to compute equivalent models for every different object available in the environment.

Phenomenological models are known to offer a good balance between realism and complexity. Models such as the one presented in [23] are built upon ground-truth output data but encompass additional physical behavior and measurement noise by using simplified equations, statistical laws and look-up tables, and implement a detection criteria based on target position and orientation relative to the sensor. This approach is also known not to be computationally expensive. Nevertheless, certain effects, such as multi-path propagation, are hard to implement only based on ground-truth data and their reproduction is not achievable.

In order to reproduce more complex phenomena linked to wave propagation, such as multi-path, interference and false-positives, radar models have employed ray-tracing technology in what is known as physical models. Still, this approach is very computationally demanding and, in some cases, the simulators are not able to ensure real-time behavior. In addition, not only these models require higher level of environment geometry detail, but they also require an additional signal processing unit, which is commonly proprietary of the sensor manufacturer and not easy to obtain.

Finally, the real models refer to over-the-air stimulation of a real radar system, based on information provided from a virtual test environment. Evidently, such a set-up requires not only hardware capable of emulating radar reflections but also a suitable place for the assembly of the whole system, as seen in [24]. One could say that these set-ups are mostly of interest of radar (or sensor) manufacturers, for performance evaluation of their components, and not for ADAS development.

For all modeling approaches, with the exception of the ground-truth model, a characterization of radar targets in the simulation environment is required. In AEB Car-to-Car tests, the task of being the surrogate target is assigned to the GVT, with its properties and characteristics better explained in Subsection 3.1.2.

3.1.2 Global Vehicle Target Characteristics

Since the surge of AEB systems in the market, a proper surrogate target for assessment tests is craved, with the general goal of being able to replicate relevant sensor characteristics, to protect the safety of the test driver, to restrain any potential damage to the VUT and be easy and fast enough to reassemble during a test campaign.

Figure 10 – The global vehicle target (GVT).

Source – Euro NCAP (2018).

The surrogate target currently used by Euro NCAP is the global vehicle target (GVT), shown in Figure 10. It is built to be an accurate representation of a passenger

vehicle, with the same visual, infrared and radar properties when seen from any direction. Its structure is designed to allow a fast assembly and a relatively low cost of repair in case of damage for replacement of parts, as shown in Figure 11.

Figure 11 – The GVT in partial assembly.

Source – Dynamic Research Institute (2020).

In a technical bulletin published by Euro NCAP [12], not only the GVT dimensions are specified, but also infrared reflectivity in key points of the body and the radar cross section are standardized. The document provides an appendix with a standard procedure for the measurement of such properties. But, despite the efforts of Euro NCAP to provide a standard and assure test repeatability, other reports evaluated the visual and radar characteristics of surrogate targets, including the GVT. These reports raised relevant technical question and proposed overall improvements.

As an example, the project “HiFi Radar Target” [25] investigated on how could the RCS of surrogate targets be assessed and compared against RCS of real vehicles. In addition, the project also suggests modification of the body of the target in order to improve the radar signature.

In [26], new methods for measurement and evaluation of soft targets are presented and a study of the target sensor signature quality is performed. At first, the report assessed the variability of optical characteristics (IR reflectivity, RGB response, u’v’ chromaticity) due to extensive use and degradation following multiple crashes, refereed as aging. The obtained results displayed small changes of optical properties over time but not enough to have an impact on the sensor identification.

Furthermore, the study carried out an evaluation of the target shape and dimension over different assemblies for a new and a used GVT, and then proceeded to

measure the shape variation due to aging. In general, the results showed strong variation of the target dimensions, up to 80 mm for different assemblies and up to 120 mm after impacts, and concluded that even a small number of impacts is sufficient to alter the body geometry. Nevertheless, if the GVT shape is in a good general shape, no major issue should appear for the camera sensor.

Lastly, the aging effect on the radar cross section of the target was investigated in [26]. Measurements were performed by circumventing the GVT with a 77 GHz radar at a range of 5.5 m to the center in order to obtain an RCS map after each impact/crash suffered by the target. In the end, the measurements acquired showed a considerable variation after each rebuild. Yet, this difference could not be directly related to the assembly, aging, or other effect on the target.

3.2 PROPOSED SOLUTION AND INTENDED GOALS

To address the topic of radar simulation for ADAS, or more specifically AEB systems, it is necessary to first of all understand the behavior of radar systems associated to the GVT. For that purpose, an investigation of radar characteristics of the surrogate target was proposed, with field measurements to evaluate its RCS and better comprehend the influence of aging upon the radar signature.

Moreover, the proposed investigation provides a good basis for the development of the functional phenomenological noisy (FPN) radar model, the main objective of this work, to replace the current ground-truth model used for functional testing.

In the next subsections, the specific requirements and goals of each part are unraveled and the proposed model structure of the FPN model is defined.

3.2.1 Global Vehicle Target Investigation

To acquire the radar characteristics of the GVT and to address and investigate the variability of its RCS due to reassembly and aging, field measurements in a test-track were proposed. The GVT used is a “Revision F” Soft Car 360°, manufactured by Dynamic Research Institute (DRI).

Located in Rodgau, the facility where most of testing takes place is formerly Opel’s test-center. Now, it operates under the administration of Segula Technologies, one of the company’s commercial partners. It offers several road layouts for the testing and validation of new vehicles, from urban scenarios to high-speed sections. The radar measurements took place in two sections, a long straight used for AEB testing and the *Skidpad*, a large plain and open area, which provides an environment with limited interference sources suited for the purpose.

The equipment used is an off-the-shelf cart also produced by DRI, designed specifically for measurement and verification of radar targets. The *radar cart*, displayed

in Figure 12, is powered by an electric motor and has automatic steering guided via differential GPS, allowing the user to precisely measure the target and relate it to range and aspect angle values. In addition, the measurements are logged in a comma-separated values (CSV) file that may be processed by DRI software or imported to MATLAB, for example.

Figure 12 – DRI Radar Cart.

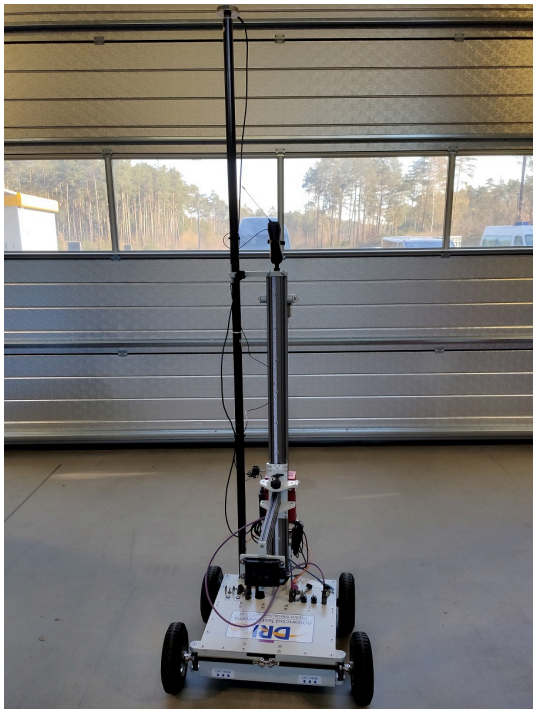

Source – Opel Automobile GmbH (2020).

Illustrated in Figure 13, different RCS measurements procedures known as fixed-angle (FA) and fixed-range (FR) were followed in two separated days. In the first day, a reference point with the available GVT was established by performing repeated FA measurements to investigate general radar effects such as clutter noise and multi-path propagation or interference, and FR measurements to acquire an initial RCS map. The second day took place after a test campaign with the GVT, so that the effects of a considerable number of impacts could be observed by performing repeated FA and FR measurements.

As the name suggests, in fixed-angle measurements the aspect angle relative to the target is fixed and the range or distance from the radar to the target varies. FA measurements are normally taken at a starting range of 100 m to 5 m, with a speed of about 1 m/s. For the proposed FA measurements of the GVT, the section of interest was the rear of the car, which is an aspect angle of $\pm 180\,°$.

The opposite is true in fixed-range measurements, with a variable aspect angle

Figure 13 – Fixed-angle (FA) and fixed-range (FR) measurement procedures.

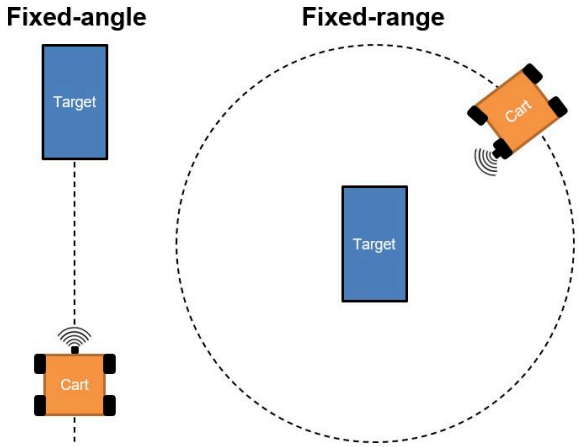

Source – Personal Archive (2020).

and a range fixed in a given value. The range was set to approximately 30 m, a typical value, and the cart was pushed in a circle around the target with a speed of 1 m/s. In summary, the required set-ups are presented in Table 1:

Table 1 – FA and FR measurements set-ups.

Procedure	Aspect Angle	Range	Sensor height	Cart speed
Fixed-angle	±180°	100 m to 5 m	0.5 m	1 m/s
Fixed-range	–180° to +180°	30 m	0.5 m	1 m/s

3.2.2 Proposed Radar Model

The desired radar model was a functional phenomenological noisy (FPN) model, build as an extension of the current ground-truth sensor available in the IPG CarMaker virtual environment, with the addition of new phenomena related to signal propagation and noise.

By obtaining ground-truth data from CarMaker's *Object Sensor*, further described in Subsection 5.1, it is possible to address the detection of traffic objects with the addition of antenna properties and target characterization parameters, such as the RCS map, to assess an estimated SNR level and compare to a set threshold, thus acquiring a phenomenological model.

This modeling approach was chosen as it is a more gradual step to enhance realism, but with a compromise to model complexity. Moreover, the modularity allowed by the FPN enables a continuous enhancement of the model as long as more know-how and experimental data are gathered in field measurements.

For better understanding, Figure 14 provides an overview of each subsystem in reality and in simulation with the proposed model, with the signal flow given from left to right of the schematic. Represented in the figure, the Bosch Perception System is a commercial solution for AEB controllers used by Opel, and it is equipped with a camera and a radar sensor, of which the information is fused into tracked object lists. Unfortunately, most of the subsystems are not accessible (black boxes) except for a preliminary object list from the radar. Yet, it allows not only reading the preliminary object list, but also overwriting it for testing purposes, thus enabling a simulation bypass.

Figure 14 – Schematic comparison between reality and proposed simulation.

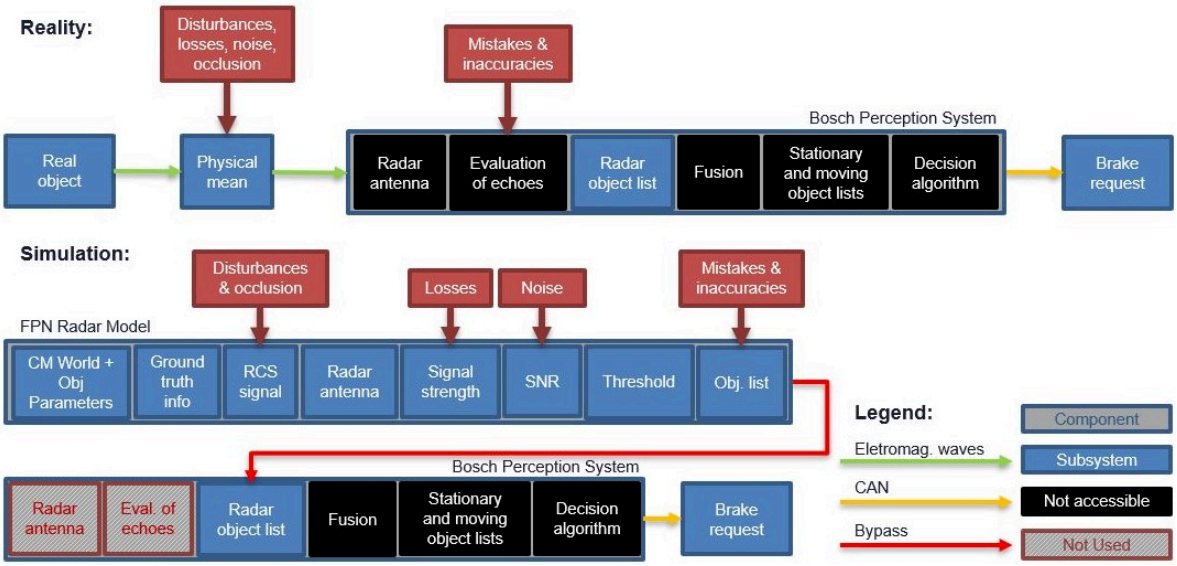

Source – Personal Archive (2020).

The FPN model had to fit the purpose of the HIL simulation and its bypass interface. So, the model was designed to have the same output quantities and data structure as required by the interface. Moreover, the radar behavior and its non-idealities present in reality were replicated in the simulation model in different subsystems. Phenomena related to the way the target is perceived by the sensor (disturbances and occlusion) were modeled on top of the RCS signal. The medium losses were applied in the signal strength calculation, noise sources were considered in the SNR evaluation and mistakes and inaccuracies related to signal processing and object tracking were added in the output object list. In summary, the proposed features of the FPN were:

- Detection based on the principle of signal-to-noise ratio considering
  - Target radar cross section (RCS);
  - Antenna gain;
  - Thermal and clutter noise;

- Occlusion;
- Detection thresholds;

- Measurement noise based on accuracy values available in datasheets;
- Simple parametrization;
- Output object list assembled with required information and structured to fit available bypass interface for hardware-in-the-loop simulators;

Figure 15 provides an overview of the cycle of the FPN model. First, information regarding each observable object position and orientation is gathered from CarMaker with the Object Sensor. Then, physical quantities, such as RCS, signal strength and SNR are evaluated to compare with the detection threshold. Finally, if the object is detectable, its output quantities are calculated and added to the object list.

Figure 15 – Overview of a calculation cycle of the FPN model.

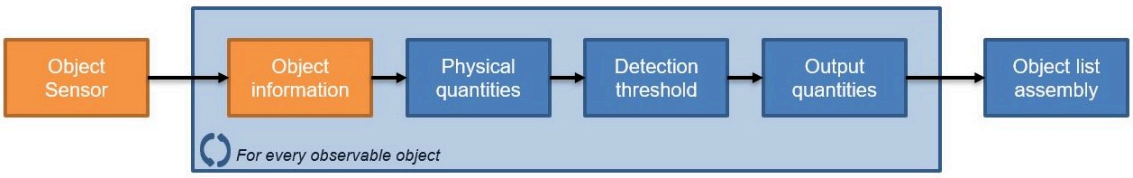

Source – Personal Archive (2020).

Model accuracy (or realism) is often linked to parametrization complexity, as briefly addressed in Section 3.1.1. Nevertheless, the FPN model had to remain easy to parametrize with data available in manufacturer data-sheets, and scenarios could not be too complex or difficult to be generated.

As a model output, vectors containing the quantities of each detected object are concatenated in a matrix of 15 rows (maximum number of configured memory address in the interface), known as the *object list*. If more than 15 objects are detected simultaneously, a rare case, objects closest to the sensor are added to the matrix. Finally, objects are deconcatenated to separated vectors and individually sent to the real radar.

3.3 FINAL COMMENTS

This chapter presented the problem description and the system requirements of the presented work. It covered the main issues regarding ADAS simulation, not only providing a literature review of radar modeling techniques, but also presenting reports that tacked the global vehicle target characteristics. In the next Chapter, the investigation of the GVT is presented.

4 GLOBAL VEHICLE TARGET INVESTIGATION

In this Chapter, the investigation of the radar characteristics of the global vehicle target (GVT) is addressed. In Section 4.1, the local where measurements took place is described and the calibration[1] procedure of the measuring equipment is explained. In Sections 4.2 and 4.3, the individual measurement results of each day are described. Finally, Section 4.4 concludes over the general results of the measurement campaign.

The most important deliverable of this chapter was the resulting plots of the RCS measurements, but, unfortunately, such plots are confidential data and had to be omitted in this version of the report. The author apologizes in advance if such an omission impairs the quality and comprehension of this chapter.

4.1 MEASUREMENT SET-UP AND SENSOR CALIBRATION

Before the execution of any measurement, a suitable location for radar measurements had to be chosen and proper calibration had to be performed to correct any noticeable inaccuracy. The next subsections present the location where the GVT measurements took place and how the calibration procedure was executed.

4.1.1 Location

In an attempt to minimize interference and noise sources, radar measurements were performed in outdoor locations in the Segula Test-center. One of the locations, the *Skidpad*, is shown in Figure 16. It could be described as a large circle, with a leveled surface, suited for any kind of maneuver. The place is free of clutter and offers great maneuvering space, allowing fixed-range (FR) measurements with a radius of more than 30 m to be performed without any issues.

The other location is a long straight section, with a width of around 15 m, located in front of the AEB hall and used for testing of such systems. For simplification, it is referenced in this text as the *AEB straight*, and it is where the fixed-Angle (FA) measurements and sensor calibration were done.

4.1.2 Calibration

Sensor calibration for the radar cart was done by executing FA measurements of a trihedral angle reflector (see 2.1.2.1.2) to obtain an offset value to be used as correction. Since the trihedral is a simple target, its RCS may be calculated using Equation (13) (for an aspect angle $\psi = 0°$), and then the theoretical value may be compared to the mean or average of the measured values. Figure 17 shows the trihedral

[1] In this document, calibration stands for the procedure to find an offset value to be applied on the recorded data to compensate for the systematic portion of the measurement error. Thus, it does not reflect the true scientific meaning of calibration, but a simplified procedure done with the radar cart.

Figure 16 – The Skidpad.

Source – Opel Automobile GmbH (2019).

provided with the radar cart. It comes with the reflector, a tripod with adjustable height and a radar absorber to “hide” the tripod.

Figure 17 – Calibration trihedral.

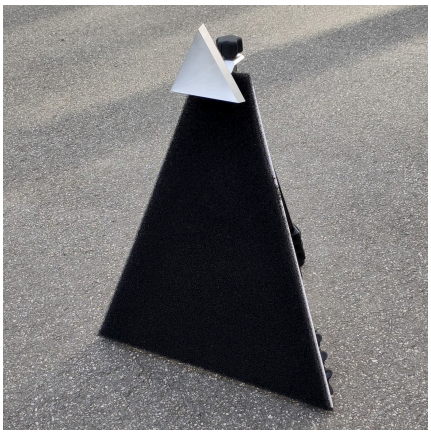

Source – Opel Automobile GmbH (2020).

The theoretical RCS of the calibration trihedral is 10 dBm^2 for a 77 GHz radar system. It was measured with three different sensor heights, 23 cm, 46 cm and 90 cm, as recommended by ISO 19206-3, in an attempt to mitigate and average out interference as much as possible. As standard in FA measurements, the cart was pushed from a distance of 100 m to 5 m to the target.

The most noticeable phenomena in the acquired results was interference by multi-path propagation, which is caused by a difference in distance traveled by the electromagnetic waves transmitted by the same sensor but propagated via different

paths (directly to the target or reflected on the ground and then to target). This multi-path propagation leads to a phase difference between the direct and indirect path waves, resulting in constructive and destructive interference. In addition to interference, the radar had difficulties to classify the trihedral as an object when in a distance greater than 70 m.

Nevertheless, the calibration offset could be obtained by using DRI Post processing software, which calculates the mean RCS value of the measurements and compares to the theoretical value.

4.2 MEASUREMENTS BEFORE TESTING CAMPAIGN

The intended goal of the first day of field measurements with the GVT was to establish a reference point for comparison with subsequent measurements after a testing campaign, when the target had experienced more collisions and the aging effect could be investigated.

4.2.1 Fixed-angle Measurements

At first, the GVT was properly assembled in the AEB straight and FA measurements were performed. The intention was to gather more data about interference patterns shown by the rear of the target ($\psi = 180°$), which is the most relevant section for the Euro NCAP AEB protocol. Simultaneously, the procedure described by the GVT Specification Technical Bulletin [12] for evaluation of the RCS was executed.

The procedure asks for FA measurements, with sensor height (h_s) of 50 cm, to be conducted in a range of 100 m to 5 m, repeated three times. It also specifies a cart speed between 3 km/h and 5 km/h and tolerance limits for lateral path deviations (< 5 cm) and angular deviations ($< 0.5°$).

The gathered data were then used in a Curve Fitting procedure for the RCS, represented by σ, with the equation

$$\sigma_{fit}(R) = \sigma_{far} - K_{dec}\min(R - R_{far}, 0)^2 \ , \quad K_{dec} > 0 \ , \tag{19}$$

where the coeficients σ_{far} and K_{dec} are to be found, R_{far} is a parameter dependent from sensor model and min(x,y) is a function whose return is the minimum value between x and y.

For the Continental ARS, one of the most common automotive radar sensors, the R_{far} parameter is 34 m. Together with R_{far}, upper and lower bounds for the curve of the ARS are also specified in [12] by the expression

$$\sigma_{bounds}(R) = 16 - 0.015\min(R - 34.0)^2 \pm 6 \ . \tag{20}$$

From the gathered data, it was possible to notice that the interference patterns seen in the calibration plots were much different that what was presented in the recorded points. This is due to a much higher number of scattering centers present in the surface of GVT when compared to the trihedral reflector. This proved to be a challenge to ensure repeatability of results, on the understanding that the slightest deviation may alter the recorded value in a given time. Even though it has proven to have high RCS values, it satisfied the bounds set by NCAP.

4.2.2 Fixed-range Measurements

All fixed-range (FR) RCS measurements were done in the Skidpad. First of all, an Opel Corsa 2020 was the target. Second, a properly assembled GVT was measured to set the standard. Third, the GVT was disassembled completely and then badly reassembled, not following manufacturer instructions and misaligning the structural pieces and cover to emulate a target in a very poor state for RCS evaluation. Finally, the GVT was reassembled properly for a second time and then measured.

The procedure was performed three times, going around the vehicle in a full circle. Next, the recorded echoes were filtered by calculating the mean value from intervals of 1 ° of aspect angle.

Even though the vehicle exterior may be regarded as longitudinally symmetric, the RCS maps displayed divergences between the left and right sides. A variety of physical effects and constructive characteristics of the vehicle, like clutter noise and statistical variations for the first, and inner components made of materials with different radar reflectivity indexes for the latter, could justify such a difference.

Next, the first properly executed assembly had no misaligned parts nor holes in its cover, and the metallic platform where the GVT is placed was carefully hidden/muffled by radar absorbing foam.

Then, the GVT was measured following the FR procedure. The RCS map obtained from the GVT of the first assembly is slightly smoother than the Corsa, which had more prominent peaks near ψ values of 0 ° (front),$\pm$90 ° (sides) and $\pm$180 ° (rear), all flatter region. In between, regions of $\psi = \pm 60°$ and $\psi = \pm 120°$ of the GVT displayed higher RCS values, mostly due to the lack of proper wheel houses to scatter the transmitted waves in multiple directions, the case of almost all passenger vehicles.

The GVT was then reassembled in a totally wrong way, with the intention to create a worst case scenario of the target, in which the staff would have no idea or experience on the assembly and assess its effect on the RCS. In this scenario, the structural pieces shown in Figure 11 were not properly aligned and the covers were left with space between them. Moreover, the cover piece representing the bumper of the car was placed upside down and the side mirrors were tilted upwards. The most aesthetically similar region was the rear side, when compared to a proper build, even

though it was also tilted to the right to a certain extent.

In general, it was expected to obtain a much more different RCS map than the previous measurement with the proper assembly. The magnitude of the recorded RCS was similar to the previous measurement, except in intervals of ψ = [–30°, –60°] and ψ = [30°, 60°], probably due to the erratic way the bumper was positioned, creating a leaned surface for a considerable extension of the GVT cover. When the radar was pointing directly to the front (0°), sides ($\pm$90°) and rear ($\pm$180°) of the target, the bad assembly RCS had little to no difference when compared to the first measurement. The average RCS value measured in the whole interval was slightly higher for the proper assembly, when compared to the bad assembly. As for the rear side (considering an interval of $\pm$2.5° from ψ = 180°), the magnitude difference was even smaller.

Closing the first day of measurements, the GVT was properly rebuilt again. This second correct assembly was done with the intention of gathering more data over the variability of results between different assemblies, regardless if the target did not sustain any damage during the period.

The gathered data have proven to be very similar to the first measurement. Generally speaking, the curve followed the same pattern, without much discrepancy in magnitude of the recorded echoes. In spite of that, the curve had some peaks at points where the first measurement was smooth and vice versa, most noticeably in the rear region (ψ = $\pm$180°). As a result, the average measured value all around and for the rear side was highest of all.

4.3 MEASUREMENTS AFTER TESTING CAMPAIGN

The second day of measurements took place after an AEB testing campaign in which the GVT had suffered a total of 10 serious impacts. Thus, it created the opportunity to investigate the aging effect upon the target, given that the previous measurements could be compared to its current status. Visually, it did not display any difference, apart from small scratches in the cover.

4.3.1 Fixed-angle Measurements

In similar fashion to the previous time, the GVT was assembled in the end of the AEB straight and, following the same FA protocol, data were gathered in three runs from a range of 100 m to 5 m and used in the Curve Fitting procedure with Equation (19).

Once again, it was possible to see that multiple scattering centers in the rear of the GVT contributed to a different interference pattern seen in the logged data. In this measurements, the radar did not detect the target at ranges greater than 80 m. That may have contributed to a lower σ_{far}, when compared to day one. Furthermore, for the

near-range decrease of RCS magnitude, K_{dec} showed almost no change, similar to the first measurements.

4.3.2 Fixed-range Measurements

With the same goal as before, the GVT was assembled twice in the Skidpad and FR measurements were performed upon them, logging the measurement for three laps around the target. Both builds were properly done in order to gather as much accurate data as possible and address the aging effect.

When compared to the other RCS maps from the first day, the overall curve had a similar shape, with the usual rounded corners in the intervals of ψ = [–60°, –30°] and ψ = [30°, 60°], and the peak values in ψ = 0°,$\pm$90° and $\pm$180°, created by the perpendicular incidence angle of the transmitted waves upon the target's surface. The average RCS value for the entire circumference was considerably lower than the first two measurements. The average for the rear side ($\pm$2.5°) was also lower in comparison to the first two proper assemblies.

Lastly, the GVT was reassembled for a second time and the FR measurements were repeated once more.The measurement results were very similar to the previous ones once again, especially when compared directly to the last. Yet, a noticeable difference in this assembly was the much shorter ψ intervals, on the sides of the car (near ψ = $\pm$90°), where the peaks of RCS magnitude used to happen. These peaks were considerably larger, and they may be due to a small deviation during the placement of the external covers of the GVT. The average RCS value for the whole interval was smaller than all the previous measurements. In contrast, the average value of the rear side was in between the two proper measurements done in the first day.

4.4 RESULTS COMPARISON AND CONCLUSION

First of all, the way the GVT is assembled has proven to be the most prominent influence in the overall results. Small tilts in a specific section of the cover, or misaligned structural pieces would cause valleys or peaks in RCS magnitude in the resulting maps when compared to other curves obtained from FR measurements. Even though all assemblies were performed by experienced staff and not with haste, the variability of the RCS map over different builds had proven to be the most noticeable result of the investigation.

The resulting RCS maps tend to have a similar shape throughout the repeated FR measurements. Still, the variation interval of the RCS magnitude cannot be disregarded, as it presents a difference of 10 dBm^2. Furthermore, the map obtained from the Opel Corsa seemed to fit in between the maps of the GVT.

In addition, something to be highlighted was the sensitivity of radar measure-

ments. Multiple variables, not only from the radar equipment used, but also the environment and the intended target, could affect the quality and repeatability of the achieved results. As an example, some measurements (FA, in special) had to be repeated a couple times because the differential GPS of the radar cart would have a small deviation in positioning and cause a “step” in the automatic steering, misaligning the radar relative to the target or creating a path error, so that the cart was not radially centered anymore, thus affecting the final result.

In the end, the results obtained were unable to provide a solid basis for any conclusion about the aging of the target. Even though the RCS measurements done in the second day (after the test campaign) displayed a small attenuation, it was not a large difference and it could not be solely related to aging, but also to the variability observed in between assemblies, as concluded by [26].

Further attention is intended to be placed upon the GVT in the near future, to acquire a better understanding not only of the target but also its direct influence in Active Safety systems such as AEB. With more gathered data, more could be said about target variability and degradation.

As a deliverable for the main objective presented in this report, the RCS maps obtained are to be used as parameters for the characterization of the traffic objects in the virtual environment, allowing the FPN radar model to consider target specific properties for the evaluation of detection.

4.5 FINAL COMMENTS

This Chapter investigated the radar characteristics of the global vehicle target (GVT), as previously proposed. Fixed-angle (FA) and fixed-range (FR) measurements were done in two days of testing, to address the issues raised in reports such as [25] and [26]. Yet, it was not possible to conclude anything on target aging. Nevertheless, the RCS data gathered was used for parametrization of the FPN model, addressed in the next Chapter.

5 PHENOMENOLOGICAL RADAR MODEL

This Chapter presents the development process of the functional phenomenological noisy (FPN) radar model for simulation of ADAS. All physical quantities addressed, together with the detection threshold and output quantities, are defined and their calculation procedure is described. The next sections are organized and divided to follow the intended signal flow, from ground-truth information to the final object list, similar to what was illustrated in Figure 14 (p. 34), in Chapter 3.

Once again, the comprehension and clarity of the modeling and implementation of the FPN radar model may be affected, given that some of the steps for the calculation of relevant physical and output quantities had to be omitted.

5.1 CARMAKER GROUND-TRUTH INFORMATION

As a database for further calculation and assessment of objects by the radar sensor, ground-truth information must be collected. IPG CarMaker, the simulation software responsible for the virtual environment, is able to provide the needed information to MATLAB/Simulink through a library of S-Functions and by using Simulink API functions. This is all set up by CarMaker (CM) automatically when a new project is generated using the “CarMaker for Simulink” option. The user only needs to use the library blocks to access the desired data.

Figure 18 shows CM library blocks used to acquire the ground-truth data about the different traffic objects present in the virtual scenario. The “Object Sensor” is omniscient of its surroundings, providing exact information about the objects, regardless of size, occlusion, or antenna behavior.

Figure 18 – CarMaker Object Sensor Library Blocks.

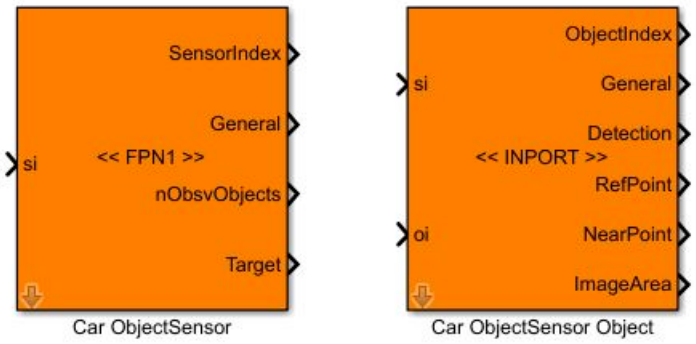

Source – Personal Archive (2020).

In the left side of the figure, the block “Car ObjectSensor” outputs information regarding the sensor itself, while the “Car ObjectSensor Object” block supplies infor-

mation regarding the traffic object. Together, they provide information about the target distance, velocity and orientation relative to the sensor frame. In addition, it delivers bearing (azimuth and elevation) and length, width and height of the object. Finally, it provides two flags, signaling when the object is in observation area (a radius of 400 m by default), and if the object is in the field of view, and thus detected.

Object information about distance, velocity, and bearing angles depend on which point of it is considered for the calculation. The outports “RefPoint” and “NearPoint”, that respectively stands for Reference Point and Nearest Point, provide the same output quantities but evaluated in a different location on the target bounding box. The Reference Point stands for the location where the object frame of reference (Fr1, in CM) is defined, usually in the back and laterally centered. The Nearest Point, as the name suggests, is the nearest point of the object bounding box relative to the sensor inside the field of view. Figure 19 illustrates the location of the Nearest and Reference Points, together with the location of the object frame of reference (Fr1) and the sensor frame of reference (FrS).

Figure 19 – Points of reference for the Object Sensor.

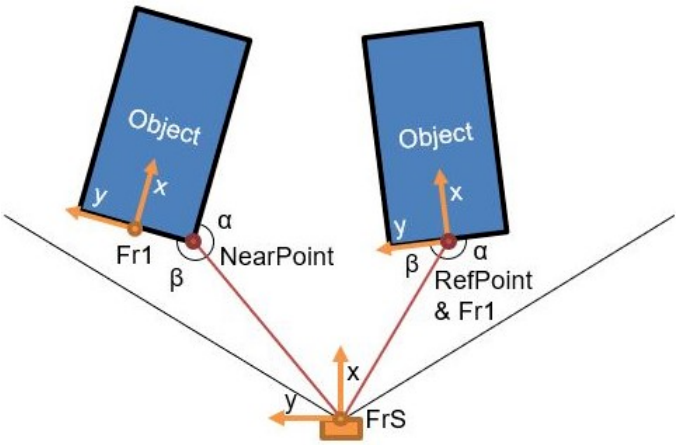

Source – Personal Archive (2020).

The outport “ImageArea” provides the degree of coverage of the sensor field of view for each object. The Nearest Point (NearP), along with the furthest left and furthest right detected point (LeftP and RightP), are projected in a horizontal plane (XY-Plane) of the sensor image area. The three projected points can range in an interval of –1 to +1, meaning left limit of the field of view and right limit of the field, respectively. In addition, incidence angles α and β on the surface of the object are calculated. These quantities available in the Object Sensor are necessary for the implementation of object occlusion or reflection of transmitted waves.

Finally, the outport “nObsvObjects” is the variable that supplies the number of observable objects (those inside the observation radius). With this information, the for-

loop presented in Figure 15 is established and the evaluation of detection is going to assess each object in the defined radius.

5.2 SIMULATED RADAR CROSS SECTION

As it was previously approached throughout this document, the radar cross section (RCS) of a target is not a simple quantity, and several different variables and factors may affect its magnitude. For the FPN radar model, a simplified RCS model is used to characterize each available target.

5.2.1 Aspect Angle Acquisition

First, the Aspect Angle ψ of the target relative to the sensor must be calculated, as it is not available directly from the data outputs of the Object Sensor block. Per definition, it is the angle between the heading axis (X-Axis) of object frame of reference (Fr1) and the line originated from the sensor origin or frame of reference (FrS) to the target center.

For the calculation, the target center coordinates, based on its dimensions, are located at the point $(x, y, z) = (L/2, 0, H/2)$ in the object frame of reference, with L for length and H for height. The center coordinates are then rotated to the same orientation as the Fr1 relative to FrS. Finally, these coordinates are translated to be defined in the FrS. With that, the distance of the target center is defined relative to the sensor origin and ψ may be acquired using the function atan2(x,y) from MATLAB. Lastly, a conversion of the function output is needed to match the usual [–180°, +180°] interval used in the previous RCS maps.

5.2.2 Seed Value and Range Dependency

The RCS maps obtained with FR measurements performed during the GVT investigation were used as parameters, correlating aspect angle and radar cross section. In CM, every traffic object defined in the test-run has a unique index, and with that, it is possible to select the RCS information related to each object, previously defined as 360-element vectors in the parameter file.

Using a look-up table, a seed value $\sigma_{lut} = f(\psi)$ for the RCS is selected. This seed is then used to model a range dependency of the target RCS, creating a σ_{ranged}, by attenuating the signal at lower ranges.

5.2.3 Signal Noise

The variability seen in radar measurements, as addressed before, is mostly due to the multi-path propagation that leads to constructive and destructive interference.

However, as discussed in Subsection 3.1.1, it is nearly impossible to properly implement such multi-path propagation phenomena without the assistance of ray-tracing techniques.

As a workaround, Gaussian Noise is added to the σ_{ranged} signal in order to generate statistical fluctuations of around 2 dBm^2, not exactly what was seen in field measurements, but still adding enough variability for object tracking. For ray-traced models, strong echoes are clustered together and later evaluated for object tracking, and a strong fluctuation of RCS values would be of smaller impact given the much larger number of evaluated echoes for a single object, in contrast to a phenomenological model, in which a small variation near a specified threshold may lead to a false-negative.

5.2.4 Object Occlusion

It is known that radar sensor are technically able to detect objects that are not direct in the line of sight (blocked by another vehicle, for example) due to multi-path propagation [19]. Yet, the measured radar cross section of the object would be impacted, and a successful detection would come to how strong the original signal was.

To replicate such phenomena in the FPN model, the “ImageArea” quantities of all objects that have a shorter distance than the current target in the X-Axis of FrS must be evaluated. The original horizontal surface size, given by the target $RightP - LeftP$, is compared to the remaining non-occluded surface to obtain a horizontal occlusion ratio O_h. In addition, the height of the target and the height of the occluding objects are also evaluated to obtain a vertical occlusion ratio O_v.

Figure 20 illustrates the projection of the ImageArea points onto the target surface. The Nearest, Left and Right Point of an object are signaled in the image for better understanding.

In the displayed scenario, Object 1 is partially occluding the left side of current target, as its projected RightP is onto the surface and it is greater than the target LeftP. On the opposite, Object 2 does contributes to target occlusion as neither LeftP or RightP are projected towards the target.

The entire analysis of objects, including the projection of ImageArea points and the evaluation of the occluded surface is done using a “MATLAB Function” block, allowing to code the intended behavior in an m-script.

5.3 ANTENNA GAIN

The antenna gain is a function G of azimuth φ and elevation angle θ. As approached in Subsection 2.1.3, in reality, the constructive characteristics of the antenna define its beam forming and thus the gain pattern and apparent field of view of the radar sensor. In the FPN model, the function $G(\varphi, \theta)$ is implemented as a look-up table.

Figure 20 – Horizontal occlusion scenario.

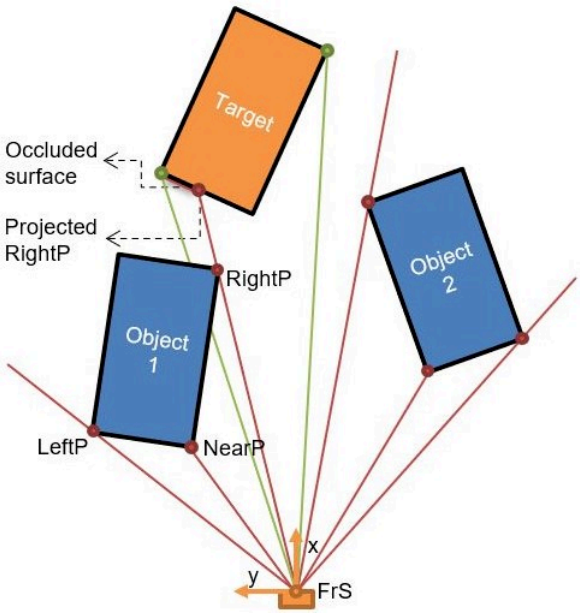

Source – Personal Archive (2020).

The map data may be generated with the aid of any external tool or by using an internal model available in CarMaker, by specifying horizontal and vertical aperture angles, and then converting the file to a MATLAB matrix afterwards. The aperture or "field of view" values for azimuth and elevation are commonly found in radar sensor datasheets.

For better comprehension, the azimuth φ and elevation θ angles are illustrated in Figure 21 as they are defined in the sensor frame of reference (FrS). In the first quadrant of the XY-Plane, φ assumes positive values, and in the second quadrant, negative values. As for θ, it assumes positive values in the first quadrant of the XZ-Plane and negative values in the second.

Figure 21 – Azimuth and Elevation in the FrS.

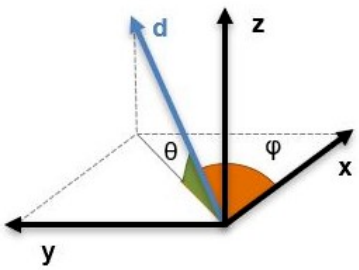

Source – Personal Archive (2020).

The “2-D Lookup Table” block, available by default in Simulink, allows the implementation of the antenna gain look-up table function, even if it is dependent of more than one variable. By properly providing table data (the gain map) and defining the breakpoints of azimuth and elevation, a complex function is simplified and implemented for similar results.

5.4 SIGNAL STRENGTH

The momentary signal strength S, for later use in the evaluation of the signal-to-noise ratio (SNR), is equal to the received power P_r, given by the classic radar equation (Equation (9)) presented in Subsection 2.1.1.

The transmitted power P_t is usually stated in radar datasheets in dBm or dBmW, but defined in Watts for the equation. In addition, λ is the wave length and R is the range to the target, both in meters. Finally, the antenna gain G and the radar cross section must be converted from its dB scale to absolute values and to squared-meters (m^2), respectively.

5.5 NOISE SOURCES

For the assessment of the noise power N in the SNR, two primary sources are considered: Thermal noise and Clutter noise. Thermal or Ohmic noise is generated by the thermal agitation of the electrons inside the circuit and it is inherent to the system. Its power is given by

$$N_{thermal} = T_a F_r K_b B_n \ , \tag{21}$$

in which T_a stands for the ambient temperature in kelvin, F_r is the noise factor[1], and it acts as a scaling factor to obtain realistic noise levels while using a theoretical approximation. Further, K_b is the Boltzmann constant in J/K and B_n is the system bandwidth in Hz.

Clutter, in radar systems, refers to the undesired echoes received by the sensor. Their sources may be irregular ground, small rocks, and even animals or insects. In a simplified way, the farther the radar sensor is from the target, greater is the clutter noise observed, as there is a larger area to the sensor.

Both sources of noise are combined simply as $N = N_{thermal} + N_{clutter}$, to obtain the final noise power in watts.

[1] Noise factor is a number by which the noise performance of an amplifier or a radio receiver can be specified. In summary, it defines the amount of noise an element adds to the overall system, and the lower the value of the noise factor, the better the performance.

5.6 SIGNAL-TO-NOISE RATIO

The detection and tracking of objects done by the FPN model is based on the concept of Signal-to-Noise Ratio. The SNR in the model is given by Equation (18), in Subsection 2.1.4.

The detection threshold is set to be a minimum signal-to-noise ratio SNR_{min}, in which its value is based on the minimum probability of detection P_{dmin} and the probability of false alarm P_{fa}, defined as parameters.

As a result of probabilistic analysis assuming a Gaussian distribution of noise, it is possible to obtain a threshold SNR_{min} to achieve the specified P_{dmin}, given a fixed probability of false alarm.

Ultimately, the overall detectability of objects presented by the radar model may be tuned accordingly with the P_{dmin} parameter, provided that reliable data from real tests are available.

5.7 OBJECT LIST

Last but not least, when all the detection evaluation is done, all the relevant information required by the bypass interface is gathered or computed and then set to be outputted.

5.8 FINAL STRUCTURE

After all modules for the calculation of physical and output quantities requested by the model were implemented, it resembled the original proposed loop, with the general Object Sensor block outside the for-loop, the assessment of each object made inside the loop and finally, the final object list done outside once more.

Some function blocks, such as the “Read CM Dict”, are not allowed to be used inside a for-subsystem. Thus, these direct variable reading blocks are placed in the “Additional CM Info” subsystem, right beneath the Object Sensor. Additionally, the RCS maps of all 15 possible objects were concatenated into a single matrix to be then sent to the FPN model and selected accordingly. Naturally, by placing it outside the for-loop there is a performance gain.

To summarize the top level of the FPN radar model: the parameters have default values and must be loaded into the model workspace. If the user wishes to modify any parameter to fine tune the model or add additional object information, he can do so. As input, it acquires ground-truth data from the Object Sensor. For that to happen, the user must configure the sensor in the vehicle configuration, inside the CarMaker Vehicle GUI and set the Object Sensor blocks in Simulink to access the information. Finally, the model provides the object list as output, containing all the necessary information for the

bypass interface. To run it, the user may simply choose a test-run in the CarMaker GUI and proceed with the simulation.

5.9 FINAL COMMENTS

This Chapter presented the implementation of the functional phenomenological noisy (FPN) radar model, the main objective of this work. It described the general concept of the model, and defined the calculation of some physical quantities, thresholds, and outputs quantities. In the next Chapter, the results of simulations are shown to validate the behavior of the FPN model.

6 RESULTS

This Chapter presents an evaluation of the developed FPN radar model based on the presentation of results. In Section 6.1, the model is compared to the phenomenological “Radar high fidelity (HiFi)” model and the ground-truth “Object Sensor” model, both available from IPG CarMaker, in different scenarios created in the virtual environment. In Section 6.2, a brief explanation of a HIL setup for AEB simulation is given, followed by the results obtained from several repeated runs in two Euro NCAP test scenarios.

6.1 OFFLINE SIMULATIONS

The purpose of the following test scenarios was to validate the behavior of the FPN model and to compare it against other available solutions. At this point, there is no controller under evaluation and only the output values of the simulated radar sensor are of interest. In the next subsections, four different test-runs created in CM are described and their results discussed.

Taken as the ego vehicle[1], an Opel Corsa 2020 simulation model developed at the company, had all three sensor models (FPN, HiFi and ground-truth) positioned in the same location, in the center of the front bumper, at a height of 0.13 m from the ground. Furthermore, the same antenna characteristics (in the case of the ground-truth sensor, an equivalent field of view) were set. Detection-related parameters, such as the minimum probability of detection and traffic object RCS, and output accuracy parameters, for distance and velocity, were also equally specified for FPN and HiFi models in order to acquire comparable data.

6.1.1 Fixed-angle Approach

The first test-run was created with the objective of displaying the behavior of the RCS of a traffic object over range, and the impact of the added measurement noise in the signals. In this scenario, the events are exactly the same as in the standard FA measurement, in which the ego vehicle approaches the target with a constant speed of 1 m/s at an aspect angle of 180 °.

Naturally, the target of choice was the GVT. It is a default traffic object available in CarMaker, as part of one of its Euro NCAP packages, with a three-dimensional (3-D) model matching the specified values. The target RCS was also parameterized, directly in CarMaker for the HiFi model, and in MATLAB for the FPN mode, using the acquired curve coming from the mean filtered data of the first assembly of the GVT on the first day of investigation.

[1] The ego vehicle refers to the vehicle equipped with the radar system.

Figure 22 displays the 3-D view of the approaching Corsa onto the GVT during the execution of the test-run. Although not relevant to radar, proper 3-D models are essential for the over-the-air simulation of camera sensors, also used in AEB systems.

Figure 22 – Opel Corsa and GVT in CarMaker virtual environment.

Source – Personal Archive (2020).

Below, Figure 23 shows the simulated RCS by the FPN model in the scenario, as a function of distance (or range) to the target. In addition, the specified upper and lower bounds for the RCS of the GVT in FA measurements were added for reference.

Figure 23 – Simulated RCS over range in FA test-run

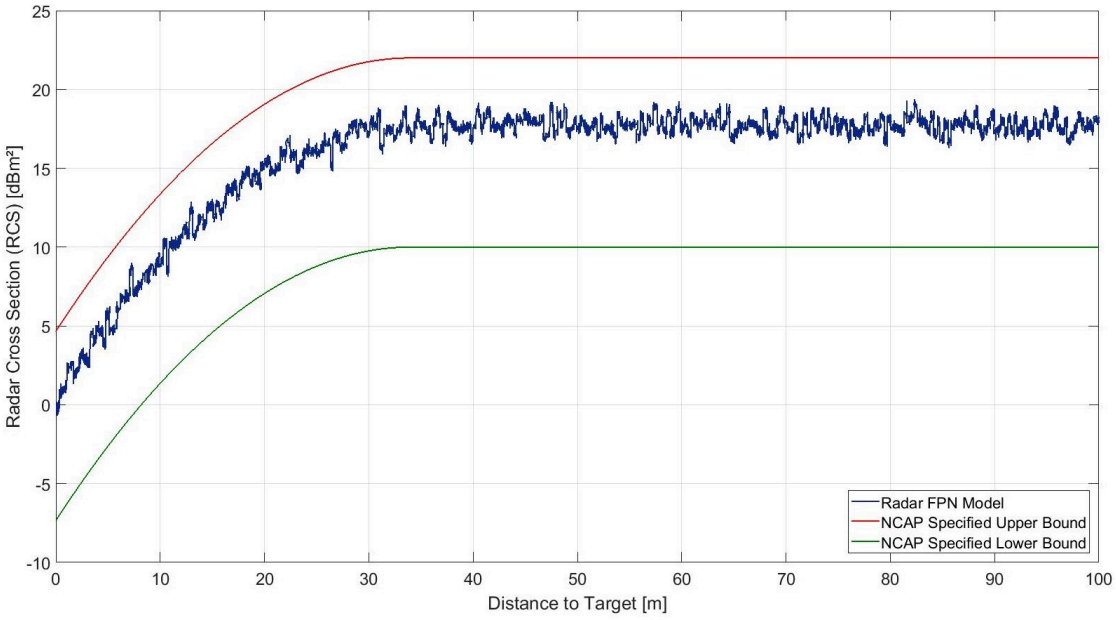

Source – Personal Archive (2020).

The RCS signal of the FPN model displayed the intended variation when Gaussian noise was added. Moreover, it showed the expected range dependency. Although the signal does not display the interference patterns seen during the GVT investigation in Chapter 4, one must bear in mind that such patterns are hardly achievable using phenomenological models, and thus raise the need for simplification on how the radar cross section of a target is implemented.

The measured velocity (the *VrelX* output in the Object List) by all three sensor models are shown in Figure 24.

Figure 24 – Measured velocity in X-Axis in FA test-run.

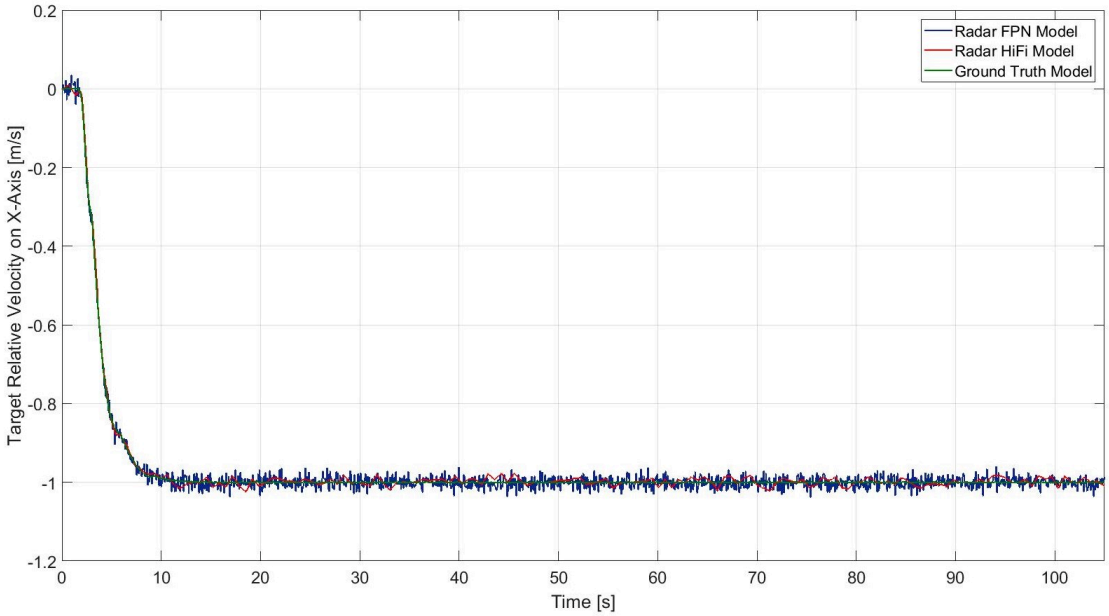

Source – Personal Archive (2020).

As expected, the velocity starts with a value of 0 m/s and then settles in –1 m/s for the remaining time of the test-run, as it is the relative velocity relative to the sensor frame and the ego vehicle is approaching the target.

As was anticipated, the ground-truth signal displayed no fluctuation or noise at all. In contrast, the FPN and the HiFi model did present measurement noise, given that both were parameterized with equal accuracy values. When compared to the “raw” noise of the FPN model, the fluctuations seen in the signal of the HiFi model are smoother, but still, similar intervals of variation were observed.

In this scenario, the target was detected during the entire execution by all models. The FA approach is an ideal situation, with the object bearing a strong RCS and directly aligned to the main antenna beam, leading to a strong signal and a high SNR value. The probability of detection in this test-run remained at 100 % at all time for both FPN and HiFi models.

6.1.2 Perpendicular Intersection

In this test-run, the ego vehicle is stationary while another vehicle crosses intersects its path from right to left-side, perpendicular to the direction the sensor is facing. The target moves forward at 5.55 m/s (20 km/h) at a longitudinal distance of 50 m. This scenario, illustrated in Figure 25, was created with the intention of evaluating the relative field of view that resulted from the antenna models, and how it affected the time interval in which the object was tracked.

Figure 25 – Proposed scenario of perpendicular intersection.

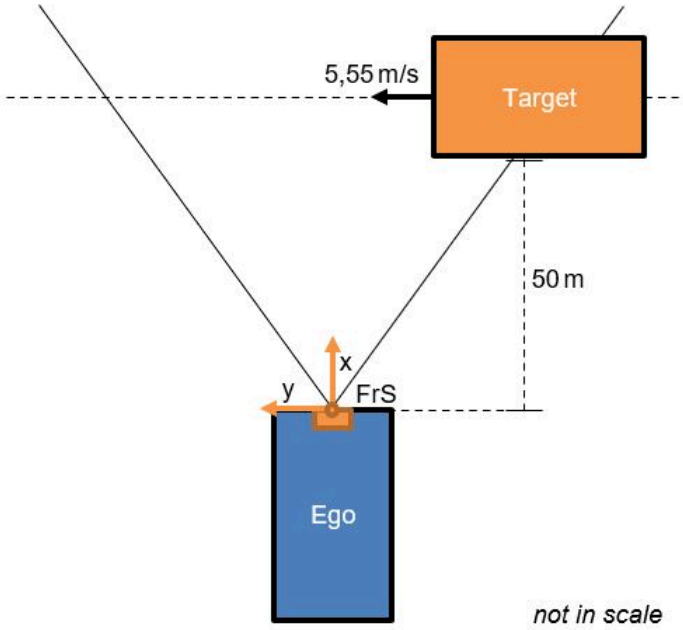

Source – Personal Archive (2020).

Not only the 3-D model of this scenario, but more importantly, the RCS map from the Opel Corsa was used for the characterization of the target, given that the vehicle also took part in one of the FR measurements performed in the first day of the GVT investigation. Similarly to the the previous test-run from Subsection 6.1.1, the RCS information resulted from the mean filtered data of the measurement.

At first, the plot from Figure 26 shows the probability of detection P_d during the execution of the test-run for the FPN and HiFi models. The latter has similar output quantities, to provide the necessary bypass signals for HIL simulation as well, being the probability of detection one of them.

The curves of both sensors displayed a similar shape, with two smaller peaks at around 5 s and 10 s, and a larger main peak in the middle. This behavior is directly associated to the fact that the antenna gain map is composed by a main lobe and several side lobes, as previously shown in Figure 5, in Subsection 2.1.3.

Altogether, the FPN exhibited a slightly larger period, in comparison to the HiFi model, where the minimum probability of detection (P_{dmin} = 0.5) was surpassed and thus the object considered as detected. This difference could be related to distinct approaches on how to model noise sources or RCS, leading to divergent SNR values.

Figure 26 – Simulated P_d in Perpendicular Intersection test-run.

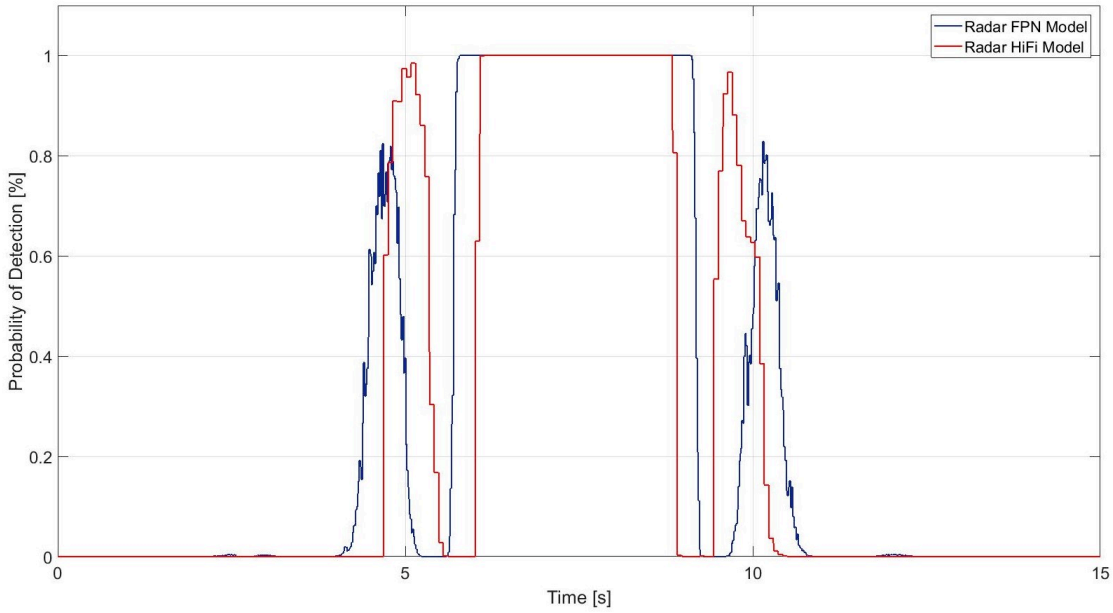

Source – Personal Archive (2020).

The absolute distances to the target, measured by all three sensor models, are shown in Figure 27. In contrast to the other sensors, which measure the distance from the sensor to the nearest point, the HiFi measures distances to the center of the object, creating the small offset value seen in the plot.

Yet, the main point of the plot is not the measured values themselves, but when and for how long was the target tracked and measured by each model. First, the FPN model tracked the target exactly during the periods for which the minimum probability was exceeded, signaling that the SNR threshold was met. Second, the ground-truth model considered the target as detectable and consequently tracked it only at the moments in which it was inside the specified field of view of $\pm 9°$ horizontally. Although the model managed to generate a similar interval of detection when considering the period of tracking “generated” by the main lobe of the antenna, it does not take into account any other condition present in the scenario. Finally, the HiFi model detected and tracked the object for a longer period than the others. The periods of detection seemed to start when P_{dmin} is surpassed, but do not exactly end after it goes down. While this is not stated in the reference manual of CarMaker, this behavior might be due to a small extension of the tracking period enabled by any state-estimation algorithm,

which is a common practice by sensor manufacturers.

Figure 27 – Measured distance to target in Perpendicular Intersection test-run.

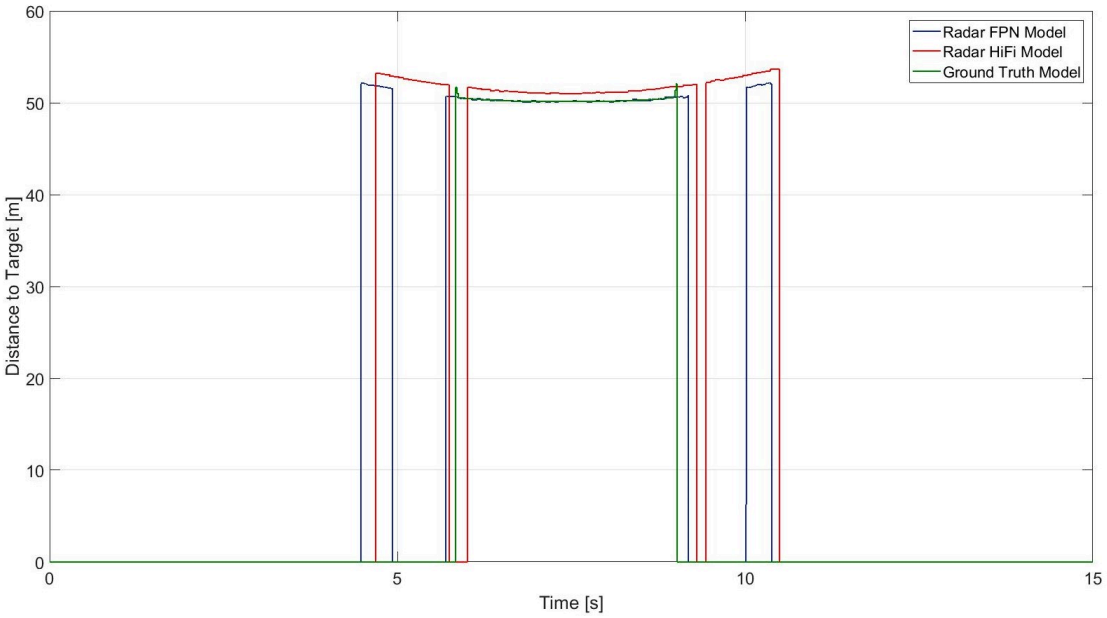

Source – Personal Archive (2020).

6.1.3 Interrupted Overtake

This test-run rehearses the scenario of an overtake maneuver, later interrupted, in a double lane highway. A set of three vehicles start to accelerate up to 50 km/h on the right lane, maintaining a 4 m gap between each other. The ego vehicle, starting 26 m away, proceeds to accelerate shortly after and reaches an equal speed of 50 km/h. Then, at $t = 25$ s the ego vehicle starts the overtake maneuver, accelerating and reaching 70 km/h. It reduces the distance to the vehicles in front until the vehicle in the middle of the group performs a lane switch maneuver at $t = 30$ s and interrupts the overtake. Lastly, the ego vehicle reduces its speed to 50 km/h again. The purpose of this test-run was to demonstrate the occlusion effect on the simulated RCS of the target and, consequently, on its detection and tracking in a realistic traffic scenario.

As shown in Figure 28, it is possible to visualize the set of vehicles at the beginning of the execution of the test-run on the top, and at the end of execution in the bottom. The targets are enumerated from #1 to #3, starting with #1 for the nearest to the ego vehicle, #2 for the middle target (that performs the lane switch), and #3 for the furthest. Additionally, one may notice that in the pictures that none of the targets is totally occluded from the sensor despite moving close to each other.

As a result, presented by Figure 29, the partial occlusion was not enough to hinder the detection of any of the targets by the FPN nor the HiFi model. The probability

Figure 28 – Scenario of interrupted overtake maneuver.

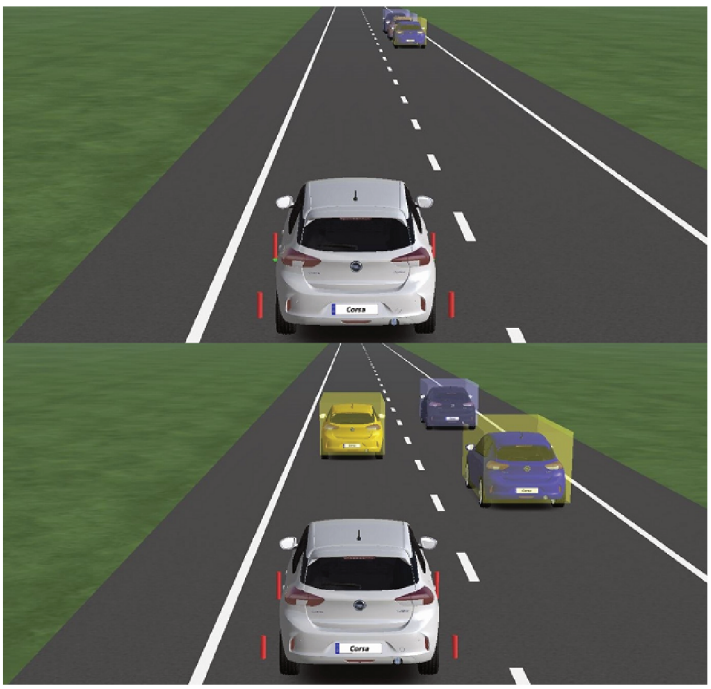

Source – Personal Archive (2020).

of detection, based on the SNR value, stays at 100% for all targets until around $t = 32\,s$, when the ego vehicle is getting closer to the targets and the lane switch maneuver is done by target #2.

Regarding target #1, the one closest to the ego vehicle, it is not occluded and has $P_d = 100\%$ for both models until it leaves the effective field of view of the sensor to a region of low antenna gain. In addition, the aspect angle of approximately $-150°$ presented by the target at this point provides smaller RCS than at aspect angles near $180°$The sum of these factors led to a sudden drop of P_d for less then a second at $t = 32\,s$, and then increasing again before lowering completely to 0% at $t = 34\,s$ for the FPN model and at $t = 35\,s$ for the HiFi model.

Target #2 remained detected for the entire duration of the execution. The lane switch maneuver done at $t = 30\,s$ only enhanced its detectability, by leaving a zone of partial occlusion into the sensor line of sight and also by displaying a region of stronger RCS when directly in front of the ego vehicle.

Affected by the lane switch maneuver, target #3 remained with $P_d = 100\%$ until target #2 moved to the left for the switch and, with that, totally occluded it. This situation, worsened by a low antenna gain at the azimuth in that moment, led to a sudden drop of P_d for both radar models, until the maneuver was completed at $t = 33\,s$.

Distances in the X-Axis, measured during the execution of the test-run, are shown in Figure 30. For all three targets, the general pattern is exactly the same, added

Figure 29 – Simulated P_d of targets in Interrupted Overtake test-run.

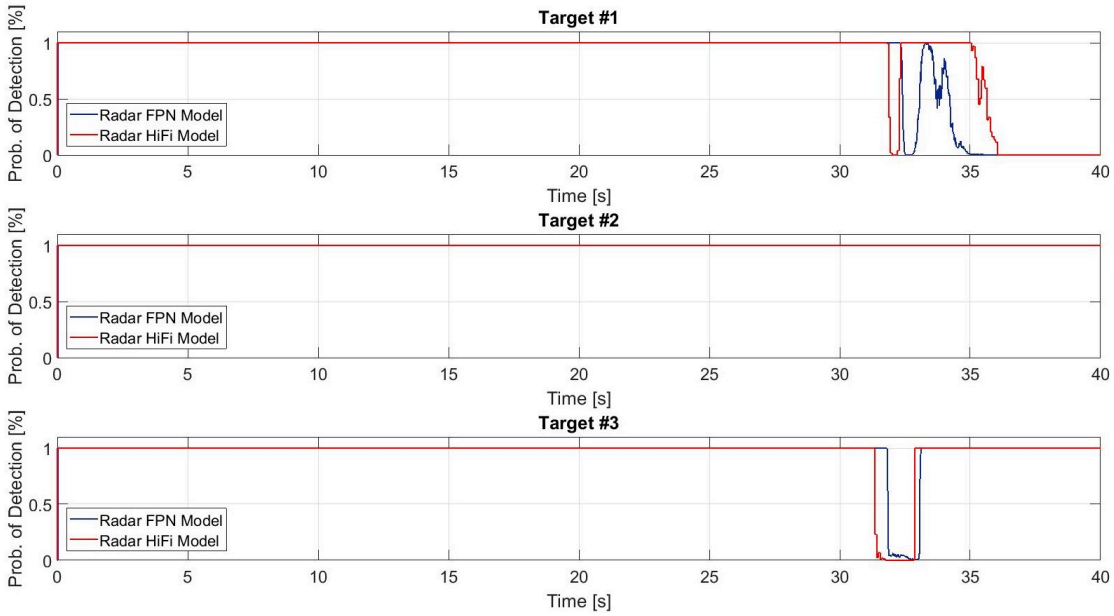

Source – Personal Archive (2020).

the offset distance of the gap between each other. The distance initially increases, given that the ego vehicle had a smaller acceleration, then it is maintained until the overtake maneuver is executed. The gap decreases before being interrupted by the lane switch of target #2. Again, it is important to point out that the difference in the measured values seen between the ground-truth and FPN models, when compared to the HiFi model, is due to the latter measures the distance relative to the object center point, and not the nearest point.

Target #1 was, once again, perfectly tracked and measured until $t = 33\,\text{s}$, when it left the effective field of view. In a first moment, the ground-truth model and the FPN model lose track of the object as the azimuth angle φ was greater than 9°, meaning the object was outside the field of view of the object sensor and it was in a low gain region of the antenna of the FPN model. While the HiFi model also experienced a decrease or oscillation in P_d at this moment, it remained tracked for a longer time, until $t = 36\,\text{s}$, resembling the behavior seen in the Perpendicular Intersection test-run of Subsection 6.1.2.

As expected, target #2 was tracked for the entire test-run. Target #3, on the other hand, was measured and tracked until the moment it was totally occluded. At $t = 33\,\text{s}$, the FPN and the HiFi model did not detect the target as the resulting SNR, and consequently the probability of detection, at that moment was below the specified threshold and the vehicle was excluded from the object list. In contrast, the ground-truth model measured and tracked the target, regardless of occlusion.

Figure 30 – Measured distance to targets in Interrupted Overtake test-run.

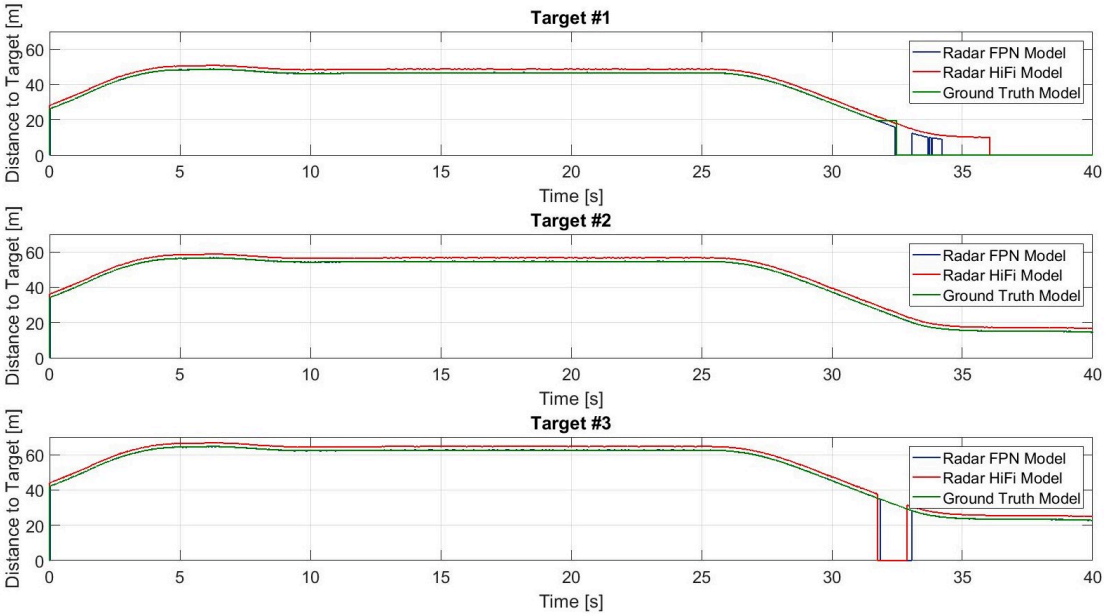

Source – Personal Archive (2020).

6.1.4 Pedestrian Crossing

The last test-run recreates a scenario of a pedestrian crossing the street, and its disposition of objects in the virtual environment is shown in Figure 31.

Figure 31 – Scenario of pedestrian crossing a street.

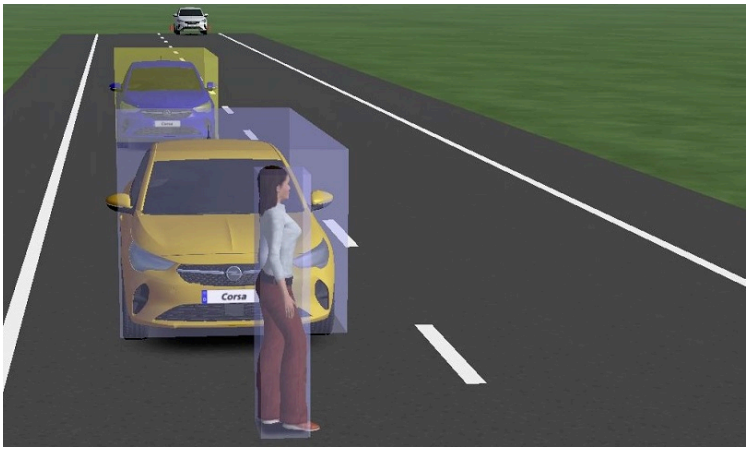

Source – Personal Archive (2020).

The pedestrian starts on the right lane (based on the direction of travel), 76 m away from the ego vehicle and totally occluded by two additional vehicles, with the closest being just 1 m behind her. The ego vehicle travels at 20 km/h on the left lane,

slowly approaching the other vehicles. Then, at $t = 12\,\text{s}$, the pedestrian completely crosses to the other side, off the road.

In this test-run, the intended goal is not only to show the occlusion effect, but also to demonstrate the impact of a considerably small RCS in the detection and tracking made by the FPN and HiFi models. The RCS map used for both models is based on simplified measurement data from different sources. In this case, the point of interest is not how accurate the map really is to characterize the pedestrian, but the effect or difference in behavior of a small radar cross section.

Again, at first, Figure 32 displays the simulated probability of detection, from the FPN and HiFi models. For both, the P_d is zero for as long as the pedestrian is occluded by the other vehicles. Then, when the pedestrian starts to move and appears to the sensor, at approximately $t = 13\,\text{s}$, the probability increases.

Figure 32 – Simulated P_d in Pedestrian Crossing test-run.

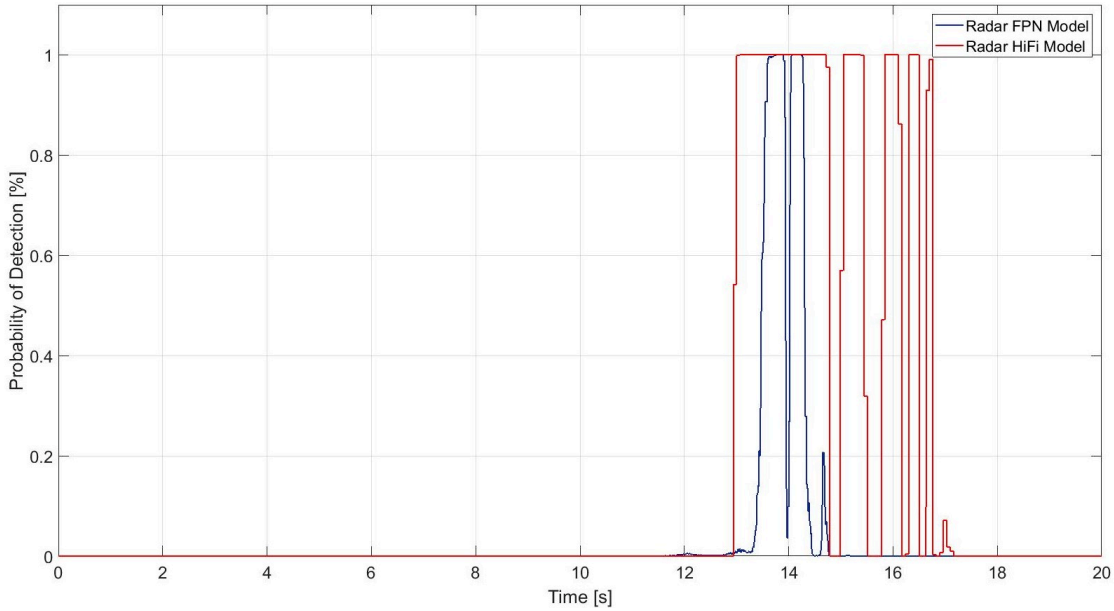

Source – Personal Archive (2020).

The FPN model shows a momentary peak at around $t = 13.5\,\text{s}$, then a valley at $t = 14\,\text{s}$ followed by another momentary (slightly smaller) peak, before diminishing to zero at $t = 14.5\,\text{s}$, the moment the pedestrian had already crosses the road and was not directly in front of the sensor anymore. On the other side, the HiFi model present a larger period of higher P_d values. It increased when the pedestrian entered the direct line of sight of the sensor at $t = 13\,\text{s}$, and remained at 100% until it left the estimated field of view. Afterwards, it oscillated between 0% and 100% until $t = 17\,\text{s}$. Altogether, both models seemed to be close to their respective SNR thresholds, with small fluctuations leading to considerable performance variation.

Next, the measured distances by each sensor model are shown in Figure 33. The distance evenly decreases as the ego vehicle moved with constant speed, until it the pedestrian was not tracked anymore, thus going to zero. The ground-truth model detected and tracked the target since the start of execution, when the pedestrian was still behind the vehicles. It only stopped detecting the target when it left the field of view ($\varphi > 9°$) near $t = 14.6\,s$. Despite the oscillations seen previously in Figure 32, the HiFi model managed to track the pedestrian for a longer period. Again, the target remained in the object list despite the low probability of detection. Finally, the FPN model detected and tracked the target strictly in the periods in which the minimum probability of detection (0.5) was met.

Figure 33 – Measured distance in Pedestrian Crossing test-run.

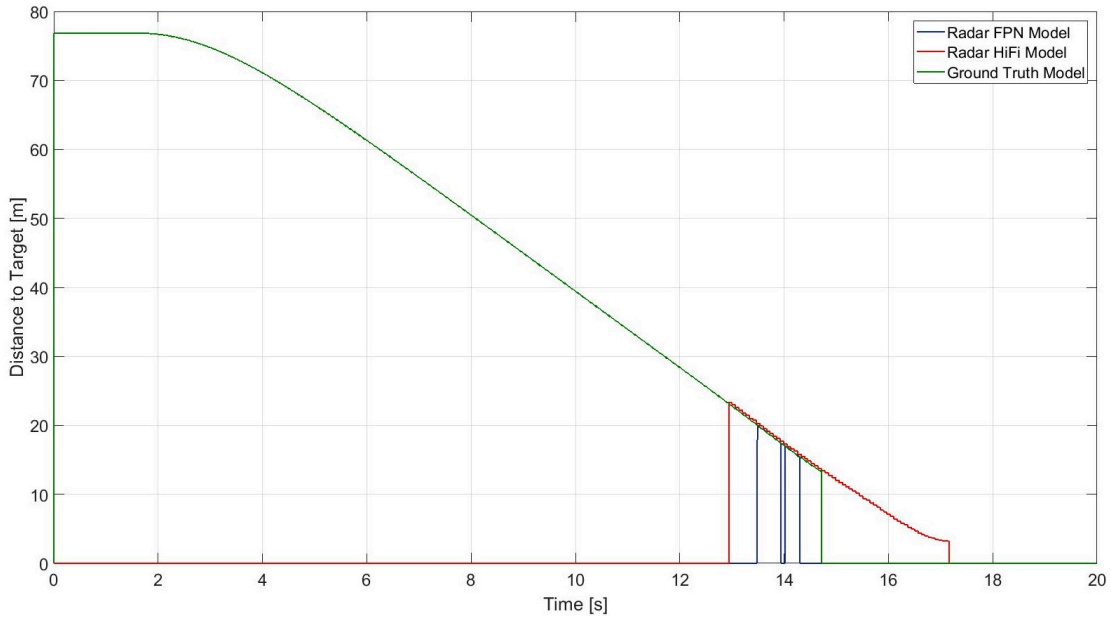

Source – Personal Archive (2020).

In general, between the phenomenological models, the HiFi presented a higher detectability of the target, tracking the target beyond the usual antenna field of view, in contrast to the FPN model, that due to the low RCS of the pedestrian, required high antenna gains to achieve sufficient SNR values.

This scenario reinforced the importance of considering target specific characteristics. A simple scenario of occlusion of a pedestrian greatly decreased the time that the object was tracked, possibly narrowing the window of an ADAS controller to recognize a dangerous situation and act accordingly.

6.2 HARDWARE-IN-THE-LOOP TESTS

In this section, the architecture of the Active Safety HIL (as it is called in the department) for simulation of the AEB systems is presented, and it is followed by a comparison[2] of results obtained in two Euro NCAP test scenarios using the FPN and the ground-truth model for radar simulation. At the time, this platform was already up and running, used for functional testing of different electronic components. Its application was only adapted by the author to test and evaluate the developed FPN radar model.

6.2.1 Simulation Platform

Hardware-in-the-loop techniques enable the engineer to test real controllers in a simulated environment. The platform is able to respond and provide stimulus to one electronic control unit (ECU) under test or more in real-time, and in this case, it also allows to close the feedback loop with a bypass of information to devices that do not have a complete simulation model available.

Figure 34 – Active Safety HIL architecture.

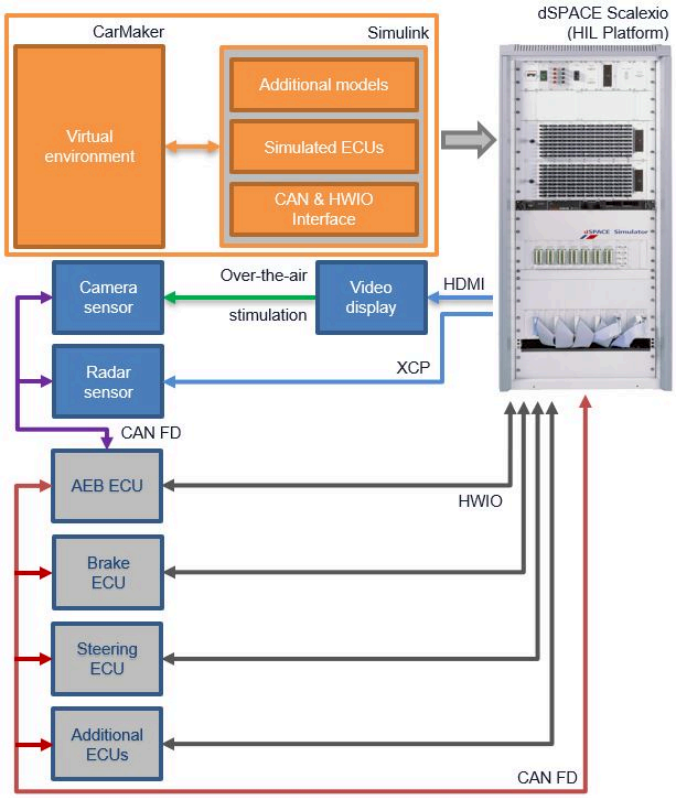

Source – Personal Archive (2020).

[2] The true performance of the AEB was masked by the usage of fictional units for distance, time and velocity, as it does not affect the main goal of directly comparing models. Instead of meters and seconds, the results shown below were converted to “unit d” for distance and “unit t” for time.

As illustrated in Figure 34, both sensors used in the AEB system (Camera and Radar) have information transmitted to them through the HIL. In the case of the Camera, the information is fed to the sensor “over-the-air” by a video display set to show the 3-D scenario from the configured position of the camera on the vehicle, in CarMaker. For the radar, the object list provided by the simulation model is injected directly into the device using a network protocol that enables read and write access to variables and memory contents at run-time called universal measurement and calibration protocol (XCP). Then, the sensors transmit their “measured” data via CAN FD to the AEB system itself, that will perform the fusion of information from each sensor, and monitor the current situation, sending a brake request to the other ECUs via a different CAN FD bus if a collision is deemed as eminent.

Systems such as Brake and Steering ECUs, also take part in the loop as real embedded hardware, as they are key components for the proper functioning of the safety feature. Hardware inputs and outputs (HWIO) are available in the platform to allow the communication between the ECUs and simulated sensors and actuators.

Additional ECU behavior may be simulated by the HIL platform to provide to the bus any other relevant CAN message that the real ECUs would expect in a normal working scenario.

6.2.2 Euro NCAP AEB Car-to-Car Test Scenarios

The performance of the AEB system was evaluated in two of the Euro NCAP test scenarios: car-to-car rear stationary (CCRs) and car-to-car rear moving (CCRm). Both protocols are performed in a similar configuration, where the vehicle under test (VUT) approaches the rear of the GVT (Aspect Angle of $\pm 180°$), in several different combinations of overlap and speed, with the latter being the differentiating factor between the two.

Figure 35 – Euro NCAP Car-to-Car Rear possibilities.

Source – Personal Archive (2020).

Figure 35 illustrates the possible scenarios of a car-to-car rear approach. In both CCRs and CCRm, the overlap may be -50%, -75%, 100%, +75% or +50% (negative overlap to the left side and positive overlap to the right side). The VUT speed ranges

may range from 10 km/h to 80 km/h between runs in the CCRs test scenario and from 30 km/h to 80 km/h in the CCRm. Finally, the GVT is stationary in the CCRs scenario, and moving at 20 km/h in the CCRm.

The CCRs and CCRm test procedures were executed ten times each in the same overlap and speed configuration in order to gather sufficient data for the performance analysis when using the ground-truth or the FPN radar model. The car-to-car rear stationary CCRs test procedure was performed with a VUT approach speed of 20 km/h and 100% overlap, and the obtained results are shown in Tables 2 and 3. The values shown in each column are measured at the moment that the AEB was triggered and the brake request sent to the CAN network. They represent calculated deltas between the measured value of the current run and the average value of all runs when using the ground-truth sensor (chosen as basis). Therefore, the values of simulation time T_{sim}, distance to target, relative velocity and time to collision (TTC) follow the equation

$$\Delta x = x_c - x_b \ , \tag{22}$$

where Δx is the difference between the current value x_c and the base value x_b, with x being either one of the displayed variables.

In this test scenario, the calculated based values were as follows: simulation time T_{sim} = 212.863 t, Distance = 85.505 d, Velocity = –4.845 d/t and TTC = 17.647 t. First, Table 2 displays the deltas of the measured values with the the ground-truth model, together with the absolute average (abs. avg.) of the results.

Table 2 – Performance deltas of the ground-truth model in the stationary scenario.

Run N.	ΔT_{sim}	Δ **Distance**	Δ **Velocity**	Δ **TTC**
#1	–0.100 t	0.075 d	0.018 d/t	0.082 t
#2	0.270 t	–0.154 d	–0.018 d/t	–0.098 t
#3	–0.047 t	0.007 d	0.005 d/t	0.021 t
#4	–0.310 t	0.100 d	0.015 d/t	0.078 t
#5	–0.011 t	0.001 d	0.001 d/t	0.001 t
#6	–0.060 t	0.045 d	0.013 d/t	0.057 t
#7	0.020 t	0.156 d	–0.002 d/t	0.024 t
#8	0.150 t	–0.106 d	–0.016 d/t	–0.080 t
#9	–0.010 t	0.014 d	0.014 d/t	0.055 t
#10	0.100 t	–0.139 d	–0.030 d/t	–0.140 t
Abs. Avg.	212.863 t	85.505 d	–4.845 d/t	17.647 t

Next, in Table 3 the deltas of the measured values with the FPN model are shown. Again, with base values from the data of the ground-truth model.

When comparing the results displayed in Tables 2 and 3, one may notice that both displayed minimum difference between each other when regarding the magnitude of the delta values. Still, the TTC (most relevant quantity) when the AEB was triggered

Table 3 – Performance deltas of the FPN model in the stationary scenario.

Run N.	ΔT_{sim}	Δ **Distance**	Δ **Velocity**	Δ **TTC**
#1	0.070 t	–0.069 d	–0.016 d/t	–0.074 t
#2	0.320 t	–0.282 d	–0.040 d/t	–0.206 t
#3	0.039 t	0.125 d	–0.003 d/t	0.013 t
#4	0.149 t	–0.123 d	–0.016 d/t	–0.086 t
#5	–0.060 t	–0.3133 d	0.069 d/t	–0.399 t
#6	0.009 t	–0.015 d	–0.016 d/t	–0.062 t
#7	–0.220 t	0.169 d	0.017 d/t	0.098 t
#8	0.120 t	0.061 d	–0.008 d/t	–0.017 t
#9	–0.180 t	–0.044 d	–0.005 d/t	–0.029 t
#10	0.050 t	–0.139 d	–0.005 d/t	–0.047 t
Abs. Avg.	212.893 t	85.160 d	–4.849 d/t	17.566 t

proved to be slightly lower in the runs with the FPN model, and when the absolute values are considered for analysis, the runs with the ideal model showed a marginally superior performance than the FPN model. In the latter, the average values were T_{sim} = 212.893 t, Distance = 85.160 d, Velocity = –4.847 d/t and TTC = 17.566 t.

Following, the car-to-car rear moving (CCRm) test scenario was performed with a VUT speed of 50 km/h and 100% overlap, approaching the GVT that is moving at 20 km/h. The results, in Tables 4 and 5, are also relative deltas to a base value taken from the average ground-truth measured data. In this case, the base values were T_{sim} = 227.393 t, Distance = 125.938 d, Velocity = –8.144 d/t and TTC = 15.463 t.

First, the resulting deltas obtained in the test runs with the ground-truth model are shown in Table 4.

Table 4 – Performance deltas of the ground-truth model in the moving scenario.

Run N.	ΔT_{sim}	Δ **Distance**	Δ **Velocity**	Δ **TTC**
#1	0.370 t	–2.986 d	–0.015 d/t	–0.394 t
#2	0.110 t	–3.408 d	0.020 d/t	–0.380 t
#3	0.070 t	–3.227 d	0.040 d/t	–0.320 t
#4	0.740 t	–3.133 d	0.055 d/t	–0.281 t
#5	–0.280 t	2.210 d	–0.012 d/t	0.248 t
#6	–0.030 t	2.393 d	–0.031 d/t	0.234 t
#7	–0.230 t	2.286 d	–0.011 d/t	0.260 t
#8	–0.310 t	1.931 d	–0.003 d/t	0.237 t
#9	–0.290 t	1.743 d	–0.014 d/t	0.187 t
#10	–0.150 t	2.192 d	–0.031 d/t	0.209 t
Abs. Avg.	227.393 t	125.938 d	–8.144 d/t	15.463 t

Bellow, Table 5 provides the resulting deltas of the test runs with the FPN model. Solely for comparison, the average values of this test scenario with the FPN model were T_{sim} = 227.500 t, Distance = 123.692 d, Velocity = –8.111 d/t and TTC = 15.248 t.

Table 5 – Performance deltas of the FPN model in the moving scenario.

Run N.	ΔT_{sim}	Δ **Distance**	Δ **Velocity**	Δ **TTC**
#1	–0.020 t	–2.799 d	0.014 d/t	–0.315 t
#2	0.060 t	–3.293 d	0.043 d/t	–0.323 t
#3	0.250 t	–3.698 d	0.021 d/t	–0.414 t
#4	0.190 t	–3.437 d	0.029 d/t	–0.367 t
#5	0.230 t	–3.452 d	0.029 d/t	–0.368 t
#6	0.150 t	–3.217 d	0.032 d/t	–0.334 t
#7	0.430 t	–3.459 d	0.001 d/t	–0.422 t
#8	0.570 t	–3.258 d	0.069 d/t	–0.270 t
#9	–0.480 t	1.911 d	0.037 d/t	0.308 t
#10	–0.310 t	2.241 d	0.042 d/t	0.358 t
Abs. Avg.	227.500 t	123.692 d	–8.111 d/t	15.248 t

Again, in general, the performance of the AEB system was slightly worst when using the FPN model, displaying a later actuation at smaller distances to the target and smaller TTCs when triggered. In this test scenario, due to the higher relative velocity, the measured values show more variability than in the stationary test scenario.

Given that in both scenarios the target is detected during the entire simulation, such difference could only be explained by the measurement uncertainties added to the model, not only directly influencing the measured data by the radar, but also affecting the integration and fusion of values with the camera. Camera sensors are not so precise for distance or range estimates, but together with radar they may complement each other to provide accurate measurements and object identification. Yet, a discrepancy between the values measured by both sensors could delay the confirmation of activation of the AEB.

Results such as those presented in the previous tables prove the importance of more complex and detailed sensor models, to allow that simulations of AEB (and ADAS in general) may be used not only for functional testing and validation, but also for assessment of system performance.

6.3 FINAL COMMENTS

This Chapter presented the results of this work. It demonstrated the behavior of the FPN radar model in offline simulations and evaluated the performance of an AEB controller in HIL simulations. The next Chapter provides the final considerations of the work done.

7 CONCLUSION

This chapter presents the final considerations and concluding remarks on the presented work. Section 7.1 summarizes the achievements, and Section 7.2 provides a future perspective of the developed project.

7.1 CONCLUDING REMARKS

In general, the presented project fulfilled the objectives defined in Section 1.3. A functional phenomenological noisy (FPN) model was fully developed and encompassed all features and characteristics listed in Subsection 3.2.2. On top of it, the model is easy to understand and parametrize, and may be further improved and extended with new phenomena and effects discovered in field testing.

In offline testing, the behavior of the FPN radar model could be validated in a set of distinct test-runs to recreate relevant phenomena, such as object occlusion, small RCS, and low antenna gain, that are seen in real traffic scenarios. In this test-runs, the model displayed similar behavior to a different phenomenological radar model (Radar HiFi from IPG CarMaker).

Further, the FPN was integrated in a HIL application with a real AEB controller, and the Euro NCAP AEB test protocols (CCRs and CCRm) were executed. To set a standard, the test-runs were also executed using the ideal radar model. In both scenarios, the resulting data pointed out slight differences in performance when using the FPN model and the ideal model, with the latter being quicker to react to the imminent collision. In these specific scenarios, this difference could be explained by the measurement uncertainties added to the outputs of the FPN.

The secondary objective, to characterize the global vehicle target (GVT), was also fulfilled. Although the investigation of the aging effect on the target was inconclusive due to the high variability of the measured radar cross section and a lack of sufficient experimental data (to address it), one of the main outcomes of the investigation turned out to be the overall similarity of the RCS maps taken from the proper assemblies and the bad assembly, intended to be a worst case scenario.

In addition, the RCS maps of the proper assemblies of GVT were successfully integrated into the simulation model in the virtual environment, characterizing the target from the perspective of the radar sensor.

To conclude, the FPN radar model, together with more advanced simulation models for camera, brakes, tires, and any other vehicle components, allow the company not only to reduce cost and time of development, but also to take a step further towards more sophisticated ADAS systems with the help of performance testing in a virtual environment.

7.2 OVERLOOK

As a future perspective of the presented work and possible improvements to the developed model, one could suggest to:

- acquire proper RCS maps for the characterization of additional traffic objects, such as pedestrians and cyclists.
- integrate additional phenomena such as
    - fog and rain damping;
    - dirt on the antenna;
    - object separability;
- improve object list quantities;
- fine-tune the detectability of the model based on field testing;
- integrate the model into more complex test scenarios;

REFERENCES

[1] PSA-Mediacenter, *Groupe psa achieved a new profitability record in 2019*, https://media.groupe-psa.com/en/groupe-psa-achieved-new-profitability-record-2019, Accessed: 07/04/2020, Feb. 2020.

[2] *Advanced Driver Assistance Systems*. Directorate-General for Transport of the European Commission, Feb. 2018.

[3] B. Fildes, M. Keall, N. Bos, A. Lie, Y. Page, C. Pastor, L. Pennisi, M. Rizzi, P. Thomas, and C. Tingvall, "Effectiveness of low speed autonomous emergency braking in real-world rear-end crashes", *Accident Analysis & Prevention*, vol. 81, pp. 24–29, 2015.

[4] Daimler-Pressroom, *20 prozent weniger auffahrunfälle durch distronic plus und bremsassistent plus*, https://www.lifepr.de/pressemitteilung/daimler-ag/20-Prozent-weniger-Auffahrunfaelle-durch-DISTRONIC-PLUS-und-Bremsassistent-PLUS/boxid/48413, Accessed: 09/04/2020, 2008.

[5] T. Unselt, J. Breuer, L. Eckstein, and P. Frank, "Avoidance of "loss of control accidents" through the benefit of esp", in *FISITA Conference, paper*, 2004.

[6] K. Bengler, K. Dietmayer, B. Farber, M. Maurer, C. Stiller, and H. Winner, "Three decades of driver assistance systems: Review and future perspectives", *IEEE Intelligent transportation systems magazine*, vol. 6, no. 4, pp. 6–22, 2014.

[7] *Assessment protocol - overall rating*, Version 9.0, European New Car Assessment Programme, Feb. 2020. available from: https://cdn.euroncap.com/media/58030/euro-ncap-assessment-protocol-overall-rating-v90.pdf.

[8] *Test protocol - aeb car-to-car systems*, Version 3.0.2, European New Car Assessment Programme, Jul. 2019. available from: https://cdn.euroncap.com/media/56143/euro-ncap-aeb-c2c-test-protocol-v302.pdf.

[9] *Test protocol - aeb vru systems*, Version 3.0.2, European New Car Assessment Programme, Jul. 2019. available from: https://cdn.euroncap.com/media/53153/euro-ncap-aeb-vru-test-protocol-v302.pdf.

[10] *Articulated pedestrian target specifications*, European Automobile Manufacturers Association, 2015. available from: https://www.acea.be/uploads/publications/Articulated_Pedestrian_Target_Specifications_-_Version_1.0.pdf.

[11] *Bicyclist target acea specifications*, European Automobile Manufacturers Association, 2018. available from: https://www.acea.be/uploads/publications/Bicyclist_target-ACEA_specifications.pdf.

[12] *Global vehicle target specification*, European New Car Assessment Programme, 2018. available from: https://cdn.euroncap.com/media/39159/tb-025-global-vehicle-target-specification-for-euro-ncap-v10.pdf.

[13] M. I. Skolnik, *Introduction to Radar Systems*, 2nd ed. McGraw-Hill, 1962.

[14] W. Wiesbeck, *Radar Systems Engineering*, 16th ed. Karlsruhe Institute of Technology, 2009.

[15] W.-K. Chen, "Editor-in-chief", in *The Electrical Engineering Handbook*, W.-K. CHEN, Ed., Burlington: Academic Press, 2005.

[16] B. Dipert, S. Poniatowski, T. Wilson, L. Kishonti, I. Riches, G. Agarwal, M. Jacobs, and D. Isaacs, *Smart exterior cameras enhance vehicle safety, security*, https://www.edge-ai-vision.com/2015/04/smart-exterior-cameras-enhance-vehicle-safety-security, Accessed: 03/08/2020, 2015.

[17] M. Feilhauer and J. Häring, "A multi-domain simulation approach to validate advanced driver assistance systems", in *2016 IEEE Intelligent Vehicles Symposium (IV)*, IEEE, 2016, pp. 1179–1184.

[18] M. R. Zofka, S. Klemm, F. Kuhnt, T. Schamm, and J. M. Zöllner, "Testing and validating high level components for automated driving: Simulation framework for traffic scenarios", in *2016 IEEE Intelligent Vehicles Symposium (IV)*, IEEE, 2016, pp. 144–150.

[19] M. Holder, P. Rosenberger, H. Winner, T. D'hondt, V. P. Makkapati, M. Maier, H. Schreiber, Z. Magosi, Z. Slavik, O. Bringmann, *et al.*, "Measurements revealing challenges in radar sensor modeling for virtual validation of autonomous driving", in *2018 21st International Conference on Intelligent Transportation Systems (ITSC)*, IEEE, 2018, pp. 2616–2622.

[20] P. Cao, W. Wachenfeld, and H. Winner, “Perception sensor modeling for virtual validation of automated driving”, *it-Information Technology*, vol. 57, no. 4, pp. 243–251, 2015.

[21] N. Hirsenkorn, T. Hanke, A. Rauch, B. Dehlink, R. Rasshofer, and E. Biebl, “Virtual sensor models for real-time applications”, *Advances in Radio Science*, vol. 14, pp. 31–37, 2016.

[22] T. A. Wheeler, M. Holder, H. Winner, and M. J. Kochenderfer, “Deep stochastic radar models”, in *2017 IEEE Intelligent Vehicles Symposium (IV)*, IEEE, 2017, pp. 47–53.

[23] S. Bernsteiner, Z. Magosi, D. Lindvai-Soos, and A. Eichberger, “Radar sensor model for the virtual development process”, *ATZelektronik worldwide*, vol. 10, no. 2, pp. 46–52, 2015.

[24] S. B. J. Gowdu, M. E. Asghar, R. Stephan, M. A. Hein, J. Nagel, and F. Baumgärtner, “System architecture for installed-performance testing of automotive radars over-the-air”, in *2018 IEEE MTT-S International Conference on Microwaves for Intelligent Mobility (ICMIM)*, IEEE, 2018, pp. 1–4.

[25] K. Karlsson, H. Toss, J. Lang, F. Costagliola, T. Zheng, and E. Marel, *Hifi radar target: High fidelity soft targets and radar simulation for more efficient testing (real and virtual)*, 2018.

[26] S. Nord, M. Lindgren, and J. Spetz, “Hifi visual target: Methods for measuring optical and geometrical characteristics of soft car targets for adas and ad”, in *Advanced Microsystems for Automotive Applications 2017*, Springer, 2018, pp. 201–209.